Published in final edited form as:

ACS Chem Neurosci. 2025 September 03; 16(17): 3292–3311. doi:10.1021/acschemneuro.5c00308.

Design, Synthesis, and Biological Evaluation of Novel Heteroaryl, Squaramide, and Indolcarboxamide Derivatives as Formyl Peptide Receptor 2 Agonists to Target Neuroinflammation

Fabio Francavilla,
Dipartimento di Farmacia-Scienze del Farmaco, Università degli Studi di Bari Aldo Moro, 70125 Bari, Italy

Daniele Vitone,
Dipartimento di Farmacia-Scienze del Farmaco, Università degli Studi di Bari Aldo Moro, 70125 Bari, Italy

Igor A. Schepetkin,
Department of Microbiology and Cell Biology, Montana State University, Bozeman, Montana 59717, United States

Lilya N. Kirpotina,
Department of Microbiology and Cell Biology, Montana State University, Bozeman, Montana 59717, United States

Antonio Carrieri,
Dipartimento di Farmacia-Scienze del Farmaco, Università degli Studi di Bari Aldo Moro, 70125 Bari, Italy

Leonardo Brunetti,
Dipartimento di Farmacia-Scienze del Farmaco, Università degli Studi di Bari Aldo Moro, 70125 Bari, Italy

Imane Ghafir El Idrissi,
Dipartimento di Farmacia-Scienze del Farmaco, Università degli Studi di Bari Aldo Moro, 70125 Bari, Italy

Maria Grazia Perrone,
Dipartimento di Farmacia-Scienze del Farmaco, Università degli Studi di Bari Aldo Moro, 70125 Bari, Italy

Corresponding Author: Enza Lacivita – Dipartimento di Farmacia-Scienze del Farmaco, Università degli Studi di Bari Aldo Moro, 70125 Bari, Italy; enza.lacivita@uniba.it;.

Author Contributions

Conceptualization: E.L. and M.L.; methodology: F.F., D.V., I.A.S., L.N.K., A.C., L.B., I.G.E., J.K.F., and E.T.; investigation: F.F., D.V., I.A.S., L.N.K., A.C., L.B., I.G.E., M.G.P., J.K.F., and E.T.; data curation: F.F., D.V., I.A.S., A.C., and E.T.; writing-original draft preparation: E.L., M.L., and A.C.; writing-review and editing: E.L., M.L., M.T.Q., and A.B.K.; funding acquisition: E.L., M.L., M.T.Q., and A.B.K. The manuscript was written through the contributions of all authors. All authors have given approval to the final version of the manuscript.

Complete contact information is available at: https://pubs.acs.org/10.1021/acschemneuro.5c00308

The authors declare no competing financial interest.

Jakub Kosma Frydrych,
Laboratory of Immunoendocrinology, Department of Experimental Neuroendocrinology, Maj Institute of Pharmacology, Polish Academy of Sciences, 31-343 Kraków, Poland

Ewa Trojan,
Laboratory of Immunoendocrinology, Department of Experimental Neuroendocrinology, Maj Institute of Pharmacology, Polish Academy of Sciences, 31-343 Kraków, Poland

Mark T. Quinn,
Department of Microbiology and Cell Biology, Montana State University, Bozeman, Montana 59717, United States

Agnieszka Basta-Kaim,
Department of Microbiology and Cell Biology, Montana State University, Bozeman, Montana 59717, United States

Enza Lacivita,
Dipartimento di Farmacia-Scienze del Farmaco, Università degli Studi di Bari Aldo Moro, 70125 Bari, Italy

Marcello Leopoldo
Dipartimento di Farmacia-Scienze del Farmaco, Università degli Studi di Bari Aldo Moro, 70125 Bari, Italy

Abstract

Recent research reveals Formyl Peptide Receptor 2 (FPR2) as a relevant G Protein-Coupled Receptor involved in the resolution phase of inflammation. Therefore, FPR2 agonists are promising agents to tackle neuroinflammatory-based diseases, such as Alzheimer's Disease or Autism Spectrum Disorder. Here, we describe the synthesis and biological evaluation of novel FPR2 agonists designed through the bioisosteric replacement of the phenyl urea function in the potent FPR2 agonist (S)-1-(3-(4-cyanophenyl)-1-(indolin-1-yl)-1-oxopropan-2-yl)-3-(4-fluorophenyl)urea (**5**), obtaining novel heteroaryl, squaramide, and indolcarboxamide derivatives. The structural modification had a profound effect on FPR2 agonist potency, metabolic stability, aqueous solubility, and cell permeability, resulting in compounds with distinct profiles. Computational studies have shown that the new compounds exhibit the same contacts with key amino acids in the binding site as the starting FPR2 agonist **5**. However, subtle differences in the orientation or the presence and position of heteroatoms in the selected scaffolds translate to substantial differences in FPR2 potency. Among the new compounds, (*S*)-**9a**, (*S*)-**12a,** and (*S*)-**16b** demonstrated neuroprotective, anti-inflammatory, and pro-resolving properties in mouse primary microglial cells, stimulated with lipopolysaccharide. Although the replacement of the phenyl urea with different scaffolds did not lead to the identification of a bioisostere, compounds (*S*)-**9a,** (*S*)-**12a,** and (*S*)-**16b** represent a starting point for the development of a new class of FPR2 agonists.

Graphical Abstract

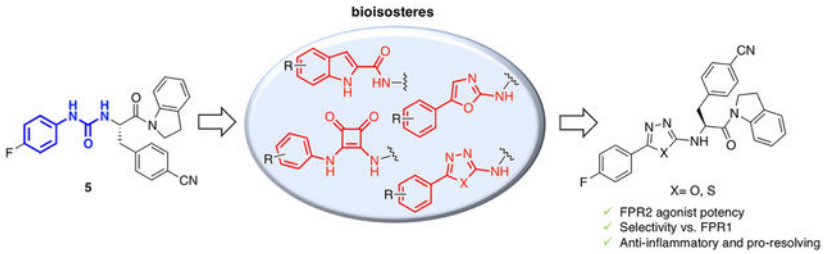

Keywords

neuroinflammation; microglia; formyl peptide receptor 2; bioisosteres; aqueous solubility; structure–activity relationships; metabolic stability

1. INTRODUCTION

Inflammation is a complex and defensive mechanism that responds to infections or tissue injury. In physiological conditions, it eliminates the initial cause of cell injury, removes damaged tissue, and promotes the restoration of tissue homeostasis. When the inflammatory response fails to resolve on its own, chronic inflammation is established, and this is the basis of a wide range of persistent and chronic diseases.[1,2] Inflammation within the central nervous system is usually referred to as neuroinflammation, and similarly to what happens in other tissues, chronic neuroinflammation contributes to tissue damage. Many neurodegenerative disorders are associated with prolonged neuroinflammation caused by overactivation of the brain's resident immune cells.[3] The resolution of inflammation (RoI) is an active and timely orchestrated process mediated by a particular class of molecules called specialized pro-resolving mediators (SPMs) with the ultimate goal of resolving the inflammatory response. SPMs are primarily derived from the oxidative metabolism of polyunsaturated fatty acids, including lipoxin A4 (LXA4), resolvins, neuroprotectins, and maresins.[4] Several lines of evidence have shown that abnormalities in SPM production and metabolism contribute to several brain disorders, and that promoting the RoI can open new therapeutic perspectives for the treatment of neurodegenerative disorders.[5,6] SPMs exert their biological effects by interacting with specific membrane receptors, including the Formyl Peptide Receptor 2 (FPR2).[7,8] FPR2 is a G protein-coupled receptor and belongs to the family of Formyl Peptide Receptors (FPRs), which also includes the FPR1 and FPR3 subtypes.[9] FPR2 is predominantly expressed in myeloid cells, such as neutrophils, monocytes/macrophages, and microglia, as well as in nonhematopoietic cells, including endothelium, smooth muscle cells, epithelium, neurons, and astrocytes.[9] FPR2 has been defined as a "promiscuous receptor" because it can be activated by structurally diverse agonists, such as endogenous lipids, proteins, peptides, and small molecules, and it can mediate opposite physiological responses based on the chemical nature of the agonists.[10,11] While the interaction with serum amyloid A or β-amyloid induces pro-inflammatory responses, anti-inflammatory and pro-resolving effects are elicited by the interaction with the SPM LXA4, resolvin D1, and annexin A1.[12,13] The underlying mechanisms of such complex pharmacology remain to be elucidated. They may involve biased signaling or receptor dimerization.[14–16]

It has been proposed that pro-resolving activation of FPR2 might potentially treat several diseases characterized by chronic inflammation, including cystic fibrosis, rheumatoid arthritis, myocardial ischemia-reperfusion, cancer, and neurodegenerative disorders.[17–19] During the past decade, several small molecule FPR2 agonists have been identified,[19] such as compound 43 (**1,** Figure 1)[20] and BMS-986235 (**2**),[21] and their anti-inflammatory and pro-resolving properties have been investigated using mainly in vitro and in vivo models of cardiovascular inflammation.[22,23] Compound ACT-389949 (**3,** Figure 1) entered phase I clinical studies, but it failed to reduce neutrophil and monocyte recruitment to the lungs following exposure to inhaled lipopolysaccharide (LPS).[24] We contributed to the field by identifying and developing a class of ureidopropanamide-based FPR2 agonists, exemplified by compounds **4**–**6** (Figure 1), having anti-inflammatory and pro-resolving properties in several models of neuroinflammation.[25,26] In rat primary microglial cells, compounds **4** and **5** were able to reduce the release of pro-inflammatory cytokines (IL-1β, IL-6, and TNF) after LPS stimulation and to induce the production of anti-inflammatory cytokines (IL-10, IL-4, and TGF-β).[26,27] In rat organotypic hippocampal cultures, compounds **4** and **5** attenuated the increase in levels of the NLRP3 inflammasome induced by LPS stimulation, suggesting that the observed anti-inflammatory effects are related to the modulation of the NF-κB/NLPR3 pathway.[28,29] In addition, microglia depletion in organotypic hippocampal cultures significantly attenuated the anti-inflammatory effects of **5**, indicating that FPR2 mediates the anti-inflammatory effects of **5** expressed on microglial cells.[29] When administered in the APP/PS1 mouse model of Alzheimer's Disease (AD), compound **4** improved neuronal survival and decreased microglial cell density and plaque load, suggesting that FPR2 activation may be a therapeutic strategy for AD.[30] Finally, chronic administration of compound **4** in two mouse models of autism reduced several inflammatory markers with a significant positive effect on social behavior.[31]

We identified compound **4** in a SAR study of the 3-(1*H*-indol-3-yl)-2-[3-(4-substituted-phenyl)ureido]propanamide scaffold. The study indicated that the 4-fluoro substituent on the phenyl linked to the urea was beneficial for FPR2 activity and that replacing the indole ring of the central amino acid core with a 4-CN-phenyl substantially improved in vitro metabolic stability.[25] In a subsequent study, fine-tuning the shape and volume of the residue linked to the amide function of **4** led to the identification of compounds **5** and **6**, two potent FPR2 agonists endowed with pharmacokinetic properties suitable for in vivo use.[26] In both studies, the urea function was left unchanged. Continuing our SAR exploration of this class of FPR2 agonists, this study evaluated the effect of replacing the urea function of the ureidopropanamide scaffold with various bioisosteres to investigate whether this structural modification affects the overall biological profile of the target compounds.

2. RESULTS AND DISCUSSION

2.1. Study Design.

The phenyl urea moiety is a privileged scaffold among FPR2 agonists.[11] The recent availability of the cryo-EM structure of the complex of compound **1**/FPR2 shed light on the interactions formed by phenyl urea derivatives within the binding site. Indeed, the urea function correctly oriented the 4-Cl-phenyl ring of **1** into a large hydrophobic subpocket

formed by residues Leu109, Phe110, Val113, Trp254, Phe257, and Phe292, which is pivotal for receptor activation. The carbonyl group of the urea engages multiple hydrogen bonds with Arg201 and Arg205, and the amine group forms a salt bridge with Asp106, thus involving amino acid residues that mutagenesis experiments suggested as crucial for the activation of FPRs.[32] Docking and molecular dynamics (MD) simulations performed on compounds **4** and **5** indicated that our ureidopropanamide derivatives established a similar pattern of interactions with FPR2.[26] In particular, the urea function of **4** and **5** established interactions with the polar amino acid residues Arg201, Arg205, and Asp106. In the present study, we have explored replacing the phenyl urea moiety with alternative scaffolds that can serve as potential bioisosteres to find groups capable of establishing the same pattern of interactions with FPR2 while improving pharmaceutical properties. Furthermore, phenyl urea contains a substituted aniline moiety, which possibly can lead to genotoxicity.[33] Therefore, inspired by isosteric replacement strategies reported in the literature,[34,35] we replaced the phenyl urea function of **5** with different moieties (Figure 2), obtaining novel compounds covering a wide range of FPR2 agonist potencies.

2.2. Synthesis of the Target Compounds.

The synthetic pathways used to obtain the target compounds are depicted in Scheme 1. The starting synthons for preparing all of the target compounds were the enantiomeric amines (*R*)- and (*S*)-**7**, which were synthesized as previously reported.[26] 2-Amino-1,3,4-oxadiazole derivatives (*R*)- and (*S*)-**9a–e** were prepared via PyBOP coupling of the amines (*R*)- and (*S*)-**7** with the appropriate 5-phenyl-1,3,4-oxadiazol-2(3*H*)-one (*R*)- and (*S*)-**8a–e**.[36] 2-Amino-1,3,4-oxathiazole derivatives (*R*)- and (*S*)-**12a–d** were synthesized starting from the amines (*R*)- and (*S*)-**7**, which reacted with thiocarbonyldimidazole to give the corresponding isothiocyanates (*R*)- and (*S*)-**10** that were condensed with the appropriate phenyl hydrazide **11a–d** in the presence of DIPEA as a base. 2-Aminooxazoles (*R*)- and (*S*)-**14** were prepared by reacting isothiocyanates (*R*)- and (*S*)-**10** with 2-azido-1-(4-fluoro-phenyl)ethanone[37] in the presence of PPh3. The squaramide derivatives (*R*)- and (*S*)-**16a,b** were synthesized by reacting the key amines (*R*)- and (*S*)-**7** with the amido-ester **15a–b**[38] via addition–elimination. Indole carboxamides (*R*)- and (*S*)-**18a–d** were prepared from amines (*R*)- and (*S*)-**7** and the appropriate commercially available indole carboxylic acids **17a–d** by using PyBOP as a condensing agent.

2.3. Functional Activity and Metabolic Stability of the Target Compounds.

The agonist activity of the target compounds at FPR2 and FPR1 was assessed by measuring their ability to induce Ca^{2+} mobilization in HL-60 cells stably transfected with human FPR2 and FPR1 and in human neutrophils (hPMN) (EC_{50}, Table 1).

We started our exploration by replacing the urea moiety of agonist **5** with 2-amino-1,3,4-oxadiazole, 2-amino-1,3,4-thiadiazole, and 2-amino-oxazole. The activity data indicated that the 2-amino-1,3,4-oxadiazole and the 2-amino-1,3,4-thiadiazole were reasonably suitable replacements for the urea moiety as the corresponding derivatives (*S*)-**9a** and (*S*)-**12a** had EC_{50} values at FPR2 in the micromolar range. In contrast, the 2-amino-oxazole was not a bioisostere of the urea moiety, because compound (*S*)-**14** was inactive at FPR2. We also synthesized and tested the (*R*)-enantiomers of (*S*)-**9a**, (*S*)-**12a,** and (*S*)-**14**, as

our previous studies indicated that FPR2 (and FPR1) could discriminate the enantiomers. We found that (*R*)-**9a,** (*R*)-**12a,** and (*R*)-**14** were inactive, in substantial agreement with the previous observations regarding the lower activity of the (*R*)-isomers at FPR2. A favorable consequence of replacing the urea moiety in **5** with 2-amino-1,3,4-oxadiazole and 2-amino-1,3,4-thiadiazole was the inactivity of (*S*)-**9a** and (*S*)-**12a** at FPR1.

In an attempt to optimize FPR2 activity, we replaced the 4-fluoro substituent of (*S*)-**9a** and (*S*)-**12a** with 4-bromo or 4-methyl substituents, which are of different sizes and/or electronic properties compared to the fluoro substituent, since the 4-bromo substituent was reported to improve FPR2 agonist potency.[39] Activity data indicated that this variation of the substituent was better tolerated in the case of 2-amino-1,3,4-oxadiazole derivatives (*S*)-**9b** and (*S*)-**9e** than in the case of 2-amino-1,3,4-thiadiazole (*S*)-**12b**. Regarding other compounds of this set, (*R*)-**9b** was inactive. Further modification by shifting the substituent on the phenyl ring from the 4- to the 3-position ((*S*)-**9a** vs (*S*)-**9c**, (*S*)-**9b** vs (*S*)-**9d**, (*S*)-**9e** vs (*S*)-**9f**, (*S*)-**12a** vs (*S*)-**12c,** and (*S*)-**12b** vs (*S*)-**12d**) led to a reduction of FPR2 agonist activity and resurfacing of FPR1 activity for (*S*)-**9c** and (*S*)-**9d**.

We continued exploring by replacing the urea moiety of compound **5** with a squaramide as a nonclassical bioisosteric replacement because of its ability to form strong hydrogen bonds and ease of preparation.[40] However, (*S*)-**16a** (i.e., the squaramide counterpart of **5**) showed a reduced FPR2 agonist activity. Replacing the 4-fluoro substituent on the phenyl ring of (*S*)-**16a** with a 4-bromo substituent improved FPR2 potency, resulting in (*S*)-**16b,** the most potent compound in this study. Regarding enantiopreference, the two pairs of squaramide enantiomers exhibited distinct behavior, as (*R*)-**16b** was inactive, while (*R*)-**16a** was equipotent to (*S*)-**16a** at FPR2. Considering FPR1 activity, three of the four squaramide derivatives exhibited low potency, while (*S*)-**16b** was inactive and, thus, highly selective for FPR2. Finally, we explored the replacement of the phenyl urea with an indole carboxamide moiety, as others have reported that the two moieties could overlap with a high degree of similarity.[41] We evaluated the unsubstituted (derivatives (*R*)- and (*S*)-**18a**), or substituted indolecarboxamides, bearing different substituents in the 5- or 6-position (compounds (*R*)- and (*S*)-**18b–d**). Overall, the data showed that this replacement was also detrimental to FPR2 activity. The presence of substituents was relevant for FPR2 activity, as the unsubstituted derivatives (*R*)- and (*S*)-**18a** were inactive both at FPR2 and FPR1, while a fluorine substituent was preferred in the 5-position ((*S*)-**18b**), rather than in the 6-position ((*S*)-**18c**). The introduction of a nitro group in the 5-position led to inactive compounds ((*R*)- and (*S*)-**18d**).

We also assessed the ability of test compounds to induce FPR2 and FPR1 desensitization by measuring the inhibition of Ca^{2+} mobilization induced by the relative standard agonists in transfected HL-60 cells or hPMN (IC_{50}, Table 1). It is well-known that FPRs can easily undergo homologous desensitization after prolonged agonist stimulation,[9] a mechanism that controls and regulates GPCR signaling and trafficking[42] and can impact the physiological responses.[43] We found that the compounds induced receptor desensitization with potency comparable to that required for receptor activation (Table 1). Next, we assessed the ability

of the compounds to induce Ca^{2+} mobilization in hPMN, and the activity data of all compounds paralleled those observed in FPR2-transfected cells.

Overall, FPR2 activity data indicated that the urea moiety is pivotal for obtaining highly potent FPR2 agonists and that the selected bioisosteres did not perfectly replicate the network of polar interactions formed by the urea moiety within the FPR2 binding site. Interestingly, the introduction of the oxadiazole and the oxathiazole rings allowed us to discriminate between FPR2 and FPR1, leading to selective FPR2 agonists.

Next, we evaluated how the replacement of the urea function with the selected potential bioisosteres impacted in vitro pharmacokinetic properties that are crucial for in vivo bioavailability, including microsomal stability, aqueous solubility, and permeability in Caco-2 cells. For each assay, we included at least one compound representative of the selected scaffolds, regardless of their functional activity at FPR2.

We assessed the in vitro metabolic stability in two steps. First, we evaluated the percentage of the parent compound recovered after 30 min of incubation with rat microsomes in the presence of an NADPH-regenerating system for the compounds with measurable activity at FPR2. Then, we determined the half-life ($t_{1/2}$) and intrinsic clearance (CL_{int}) of the compounds with a recovery percentage higher than 15% in the first assessment (Table 2). The tests indicated that the selected bioisosteric replacements have different impacts on metabolic stability. For instance, indole carboxamide derivatives exhibited substantially improved metabolic stability compared to **5**, with (*S*)-**18c** being the most stable compound in this study ($t_{1/2}$ = 105 min). The metabolic stability in vitro of the squaramide derivatives seemed to depend on the phenyl ring substitution, as the 4-Br-substituted derivative (*S*)-**16b** had a half-life value more than 2-fold higher than that of the 4-F-substituted analog (*S*)-**16a**. Finally, replacing the urea moiety with 2-amino heteroaryl rings impacted the metabolic stability to different extents as the compounds had half-lives ranging from 14 to 47 min. The thiadiazole derivative (*S*)-**12a** exhibited the best combination of FPR2 activity and in vitro metabolic stability within the 2-amino heteroaryl bioisosteres.

Overall, divergent requirements affect the FPR2 activity and metabolic stability in this set of compounds. Structural modifications that sustain FPR2 agonism reduce metabolic stability and vice versa.

Regarding kinetic aqueous solubility, we studied selected compounds to probe whether the bioisosteric replacement positively affected this property (Table 2). We first assessed the kinetic solubility of 5, which had low aqueous solubility (S = 10.5 μM). Next, we evaluated the kinetic solubility of the 2-amino-1,3,4-oxadiazole derivatives (*S*)-**9a**, (*S*)-**9b**, and (*S*)-**9e**, the 2-amino-1,3,4-thiadiazole derivative (*S*)-**12a,** the 2-amino-oxazole derivative (*S*)-**14**, the squaramides (*S*)-**16a** and (*S*)-**16b,** and the indole carboxamide (*S*)-**18b**. The data showed that only the squaramide derivatives (*S*)-**16a** and (*S*)-**16b** have an aqueous solubility comparable to **5**, suggesting that hydrogen-bonding donor groups are necessary for solubility. On the other hand, introducing amino-heteroaryl or indole carboxamide moieties reduced the number of hydrogen-bonding donor functionalities, resulting in a substantial decrease in aqueous solubility.

Finally, we assessed apparent permeability coefficients (P_{app}) across a Caco-2 cells monolayer for compounds **5**, (*S*)-**9a**, (*S*)-**12a**, (*S*)-**14**, (*S*)-**16b,** and (*S*)-**18b** as a measure of the ability of compounds to permeate the blood–brain barrier. Caco-2 cells form tight junctions and express efflux transporters of the ATP-binding cassette superfamily, including *P*-glycoprotein (*P*-gp). Thus, Caco-2 is a valuable in vitro model for gaining information not only on a compound's passive permeability across the cell membrane but also on its interaction with efflux transporters.[44] For the selected compounds, we assessed the P_{app} across the cell monolayer in both directions, from basolateral to apical (BA) and from AB direction, and the ER between BA and AB fluxes (Table 2). ER greater than 3 is predictive of undesirable interaction with the efflux transporters and, thus, of limited brain permeation.[45]

We found that all compounds exhibited good permeation rate from the basolateral to the apical direction, suggesting that the compounds can diffuse passively across the cell membrane. Instead, we observed very different P_{app} values in the apical to basolateral (AB) direction, which is strongly influenced by the interaction with efflux transporters, as reflected by the calculated efflux ratio (ER) values. We can note that all compounds showed ER values greater than 3. On one hand, compounds **5** and (*S*)-**9a** had ER values of 4.4 and 3.8, respectively, which suggested sufficient membrane permeability and a moderate interaction with the efflux pumps. On the other hand, compounds (*S*)-**12a,** (*S*)-**14**, (*S*)-**16b,** and (*S*)-**18b** exhibited very high ER values, indicating a strong interaction with the efflux transporters and, consequently, limited cell permeability.

2.4. Computational Studies.

To gain insight into how the target compounds interact with FPR2, we performed computational studies using the available cryo-EM structure of the human FPR2 complex with the fMLFII peptide and Gi2 (PDB ID: 7WVV).[46] First, we used docking studies to compare the binding mode of the most representative target compounds, namely, (*S*)-**9a**, (*S*)-**12a,** (*S*)-14, (*S*)-**16b,** and (*S*)-**18b,** with that of 5. The compounds generally had similar docking poses and interaction patterns within the binding cavity (Figures 3 and S1). Considering (*S*)-**9a** as representative of this new series of FPR2 agonists, docking studies evidenced that the cyanophenyl and the indoline rings are critical pharmacophoric points forming aromatic π–π stackings (*edge-to-face* to Phe292 and *face-to-face* to Phe178 and His102, respectively). With similar merit, a charge transfer complex engaging the guanidinium terminal of Arg201 and π–π stackings of the 4-fluorophenyl ring with Phe110 and Trp254 were observed. Intriguingly, the formation of an extended water-mediated hydrogen bond network recruiting the heterocyclic moiety of (*S*)-**9a** and the Arg205 side chain was observed. We observed additional polar interactions consisting of a second water molecule, which contacts the cyan group and Asn285, and a unique "NH–π" contact made by Glu258 and the 4-fluorophenyl ring deeply buried within the transmembrane segment (Figure 3).

Docking scores for the selected agonists expressed through the ESP rule (see Section 4) validate the described binding mode (Table 3).

To further validate the docking predictions and establish the pharmacophore model as a robust tool for inferring experimentally acquired efficacy data and supporting structure–activity relationships, we subjected the ligand poses docked in the FPR2 binding site to Prime Molecular Mechanics Generalized Born Solvent Approach (MM-GBSA).[47]

Remarkably, we observed a notable trend ($r^2 > 0.4$) in the correlation between activity data and in-silico ΔG predictions (Table 4).

However, upon a thorough examination of the data distribution and employing a leave-one-out procedure, the correlation significantly improved, with r^2 rising to 0.923 after excluding the pronounced outlier 5. This compound, indeed, is the sole ureidic derivative within this set, further emphasizing its deviation from the overall trend.

Next, we performed MD simulations to verify the temporal occurrence of the set of contacts that most likely governs the binding interaction and the observed differences in ligand potencies. The dynamic trajectories were produced using the six FPR2-complexes docking poses as input. To facilitate data mining, histogram plots showing the various types of ligand–receptor interactions and their relative occurrences were extracted from each trajectory, as reported below (Figure 4).

The results showed that in almost all MD simulations, the most relevant and persistent receptor interactions involved charged amino acids such as Asp106 (even with the help of a water molecule), Arg201, and Arg205, which mainly engage the polar core of the ligands. The 4-fluoro- or 4-bromophenyl rings recruited the aromatic residues Phe110 and Phe257, producing significant contacts in the deepest and most buried segment of the transmembrane helices bundle.

As the free energy of binding was able to rationalize the pEC_{50} data, we derived further insights into the structure–activity relationship from three additional geometric descriptors sampled during the last 600 ns of the dynamics runs. These descriptors encode the contact surface area (CSA), calculated as the solvent-accessible surface area of the complex minus the solvent-accessible surface areas of the FPR2 receptor and the ligand, respectively, the distance (CoM) measured on the barycenter of the two distinct molecular entities, and the Radius of Gyration (RoG) of protein–ligand complexes. These metrics provided further understanding of the interactions and spatial arrangements within the binding site, contributing to a more comprehensive view of the structure–activity relationship (Table 5).

We observed some very interesting hints while correlating the efficacy data with the statistical figures (i.e., mean, standard deviation, and range), showing the trend of these descriptors. In details, the CSA, intent as the shape or extension of molecular interactions eventually changing during the dynamics run and accounting then also for flexibility and/or stability of the receptor ligand complex, resulted slightly ($r^2 = 0.577$) able to interpret pEC_{50} in just one instance, the range, and considering as outlier (*S*)-**18b,** and an even more obscure view was achieved in the case of CoM, encoding information relative to fluctuations or structural stability, able to produce sound ($r^2 = 0.790$ with mean values) statics only if **9a**, and **14** are excluded for the data set. Nonetheless, a much more straightforward interpretation of the difference in ligands efficacy indeed emerged by the

correlation between pEC_{50} and RoG, as expression of compactness and tighter molecular interactions and therefore a more favorable binding, since in all the three combinations relevant correlations were gain, specifically $r^2 = 0.619$ with mean, $r^2 = 0.830$ with standard deviation, and $r^2 = 0.931$with range values. Importantly, we derived these statistics by excluding compound **5** from the correlation analysis.

Then, among the evaluated structural descriptors, RoG was more relevant for the correlation and interpretation of structure–activity relationships, as well as for summarizing the dynamics runs' conformational stability and spatial organization, than CSA and CoM. An additional interpretation and validation might also be perceived from the timeline and whisker plots of RoG fluctuations reported in Figures S2 and S3.

As a further proof of concept, the results of K-means Clustering and Principal Component Analysis, carried out with RoG values, propose a reasonable picture of ligand efficacy. The 3D scatter plot reported in Figure 5 shows a well-defined spatial separation, in three different clusters, of compounds in PCA space according to their efficacy, with most active compounds (*S*)-**5** and (*S*)-**16b** located at the extremes of PC1, moderate efficacy ligands (*S*)-**9a** and (*S*)-**12a** projected on PC2 axis, while less active derivatives (*S*)-**14** and (*S*)-**18b** cluster opposite on PC3.

While docking studies did not catch substantial differences in the binding mode of **5** and bioisosteres, the analysis of the MD simulations evidenced subtle differences among the compounds that could be attributed to the agonist potency of the compounds. Thus, we believe this approach could support further refinement of the bioisosteric replacement of the phenyl urea function.

2.5. Effect of Selected FPR2 Agonists on Cell Death and Nitric Oxide (NO) Release in Mouse Primary Microglial Cells.

We assessed the effect of (*S*)-**9a**, (*S*)-**12a,** and (*S*)-**16b,** which featured the highest FPR2 agonist potency in this study, on cell death in mouse primary microglial cell cultures under basal conditions or after stimulation with nonspecific immune activator LPS. We used the lactate dehydrogenase (LDH) assay, a widely recognized method for quantitatively measuring cell death due to plasma membrane damage. LPS is known to compromise the cell membrane integrity, increasing LDH efflux from damaged cells. The specificity of the observed effects was assessed by pretreating primary microglial cells with selective FPR2 antagonist WRW4.

None of the tested compounds elicited a notable increase in the level of LDH release under basal conditions. Exposure to LPS (0.1 μg/mL) resulted in a pronounced upregulation of LDH release ($p = 0.008803$, Figure 6A; $p = 0.002954$, Figure 6B; $p = 0.003135$, Figure 6C), indicative of significant cell damage. The FPR2 agonists (*S*)-**9a** and (*S*)-**12a** (1 μM) demonstrated protective effects by effectively mitigating the LPS-induced cytotoxicity ($p = 0.0011031$; $p = 0.014069$, respectively). Pretreatment with WRW4 (10 μM) blocked this effect only in the case of (S)-**9a** ($p = 0.011842$, Figure 6A).

Next, we investigated the impact of the selected FPR2 agonists on NO production, both under basal conditions and after LPS stimulation. Glial cells produce NO in response to inflammatory signals, and excessive NO levels can worsen neuroinflammation, leading to neuronal death and tissue damage.[48] Microglia cells stimulated with LPS exhibited significantly increased NO production ($p < 0.0001$, Figure 7A; $p < 0.0001$, Figure 7B; $p < 0.0001$, Figure 7C). Pretreatment with (*S*)-**9a** and (*S*)-**12a** (1 μM) effectively attenuated LPS-induced NO production ($p < 0.0001$, and $p = p < 0.0001$, respectively, Figure 7A,B). Notably, pretreatment with WRW4 (10 μM) blocked effects evoked by the FPR2 agonists ((S)-**9a**: $p < 0.0001$, (S)-**12a**: $p < 0.0001$; Figure 7A,B).

2.6. Effect of Selected Target Compounds on the Levels of Pro-inflammatory and Anti-inflammatory Factors in Mouse Primary Microglial Cells.

To elucidate the anti-inflammatory and pro-resolving properties of the selected FPR2 agonists, we evaluated their impact on the production of proinflammatory cytokines IL-1β, IL-6, and anti-inflammatory cytokine IL-10. We also included the evaluation of the effect of compounds on IL-33, a recently discovered multifunctional member of the IL-1 family, that mediates both pro- and anti-inflammatory effects, playing a complex role in neurodegeneration.[49] IL-33 regulates microglial responses and is required for microglial phagocytic processes and migratory activity. The dual role of IL-33 in microglial M1/M2 phenotypic changes and secretion of inflammation-related cytokines explains why IL-33-reactive microglia exhibit diverse inflammatory responses under different conditions or even in the same disease.[49] However, the involvement of IL-33 in the functional expression of microglia is poorly understood. For all cytokines, we assessed the effects both under basal conditions and after LPS stimulation. The FPR2 antagonist WRW4 was used to determine the specificity of the observed effects.

Interestingly, none of the studied compounds induced a significant effect on the levels of the studied cytokines under basal conditions, suggesting that the compounds did not induce pro-inflammatory effects. Stimulation with LPS (0.1 μg/mL) significantly increased IL-1β, IL-6, IL-33, and IL-10 levels measured in the medium of microglial cultures ($p < 0.0001$; $p < 0.0001$; $p = 0.012392$; $p = 0.000152$; respectively, Figure 8A–D). Compound (*S*)-**9a** (1 μM) decreased the levels of all cytokines in LPS-stimulated microglial cultures ($p < 0.0001$; $p < 0.0001$; $p = 0.025320$; $p < 0.0001$, respectively, Figure 8A–D). The observed effects on IL-1β, IL-6, and IL-33 were mediated by the interaction with FPR2 because they were abolished by pretreatment with WRW4 (10 μM) (IL-1β: $p = 0.000152$; IL-6: $p < 0.0001$; IL-33: $p = 0.007358$; Figure 8A–C).

(*S*)-**12a** exhibited similar anti-inflammatory effects as (*S*)-**9a**. LPS stimulation (0.1 μg/mL) induced a significant upregulation of the production of all the studied cytokines (IL-1β: $p < 0.0001$; IL-6: $p < 0.0001$; IL-33: $p = 0.001402$; IL-10: $p = 0.000150$; Figure 8A–D). Notably, (*S*)-**12a** (1 μM) decreased IL-1β, IL-6, and IL-33 levels was observed ($p < 0.0001$; $p < 0.0001$; $p = 0.001402$; respectively), while no statistically significant effect was observed on IL-10. Pretreatment with WRW4 (10 μM) abolished the effect only on IL-1β and IL-6 release (IL-1β: $p = 0.000162$; IL-6: $p < 0.0001$; Figure 9A,B).

Compound (*S*)-**16b** provided outcomes comparable to those observed for (*S*)-**12a**. Again, after LPS stimulation (0.1 μg/mL), significant increases were observed in the levels of IL-1β ($p < 0.0001$), IL-6 ($p < 0.0001$), and IL-10 ($p < 0.0001$) (Figure 9A,B,D). Pretreatment with (*S*)-**16b** (1 μM) effectively diminished LPS-induced IL-**1β** ($p < 0.0001$), IL-6 ($p = 0.00152$), and IL-10 ($p < 0.0001$) release (Figure 10A,B,D, respectively). These effects were abolished by pretreatment with WRW4 (IL-1β: $p = 0.000152$; IL-6: $p < 0.0001$; IL-10: $p = 0.00152$; Figure 10A,B,D, respectively). Conversely, the levels of IL-33 were affected by neither (*S*)-**16b** nor WRW4 (Figure 10C).

Considering that FPR2 can mediate both pro- and anti-inflammatory effects and that the structural modifications targeted the urea function, which is pivotal for the molecular interaction of the molecule with the receptor, these data indicate that bioisosteric replacement of the urea did not alter the anti-inflammatory and pro-resolving properties of our FPR2 agonists. Indeed, the studied compounds could counterbalance LPS-induced cytotoxicity and release of proinflammatory and anti-inflammatory cytokines, albeit in a different manner. Interestingly, this is the first study demonstrating that the FPR2 activation may modulate the levels of IL-33 in activated microglia, offering new pieces of evidence in the regulatory role played by IL-33 plays in the microglial functional state.

3. CONCLUSIONS

FPR2 agonists have shown efficacy in several disease animal models characterized by chronic inflammation, including neurodegenerative disorders, and they have the potential to treat a range of diseases. Phenyl urea is a recurring scaffold embedded in most synthetic FPR2 agonists. It is responsible for the most efficient orientation of the molecule within the FPR2 binding site by forming polar interactions with key amino acid residues, i.e., Arg201, Arg205, and Asp106, which are responsible for anchoring the molecule. Starting from our potent FPR2 agonist **5**, we wanted to further explore the structure–activity relationships of this class of FPR2 agonists by replacing the urea moiety with different bioisosteric scaffolds and see if this structural modification could improve the pharmaceutical profile of the molecule. In addition, phenyl urea contains an aniline moiety that could raise genotoxicity-related issues. We synthesized novel heteroaryl, squaramide, and indolcarboxamide that showed lower FPR2 agonist potency than starting agonist **5,** thus confirming the pivotal role of the contacts established by the phenyl urea moiety in the binding site. On the other hand, the structural modification improved the selectivity of the compounds over FPR1. The bioisosteric replacement of the phenyl urea moiety led to compounds with different profiles regarding metabolic stability, aqueous solubility, and cell permeability. The indole carboxamide derivatives (*S*)-**18b**,**c** were three-to four-fold more stable toward oxidative metabolism than **5**, whereas compounds (*S*)-**9a**,**c** were rapidly metabolized. On the other hand, the oxadiazole derivative (*S*)-**9a** showed a slightly improved cell permeability profile as compared to **5**. In contrast, compounds bearing the other scaffolds showed very poor cell permeability because of their strong interaction with the efflux transporters. Computational studies highlighted that the new derivatives shared docking poses within the FPR2 binding site similar to **5**. Yet, subtle differences in the orientation of the phenyl ring or the presence and position of heteroatoms in the selected bioisostere moieties accounted for substantial differences in FPR2 potency. Among the studied compounds, the FPR2 agonists

(*S*)-**9a**, (*S*)-**12a,** and (*S*)-**16b** underwent further characterization of their neuroprotective, anti-inflammatory, and pro-resolving properties in mouse primary microglial cell cultures under basal conditions and after stimulation with LPS. All of the selected FPR2 agonists counterbalanced LPS-induced cytotoxicity. They modulated the release of both pro- and anti-inflammatory cytokines, and the effects were FPR2-mediated because they were abolished by pretreatment with the antagonist WRW4.

To conclude, the replacement of the phenyl urea with alternative scaffolds led to the identification of FPR2 agonists with a very different profile as compared to the agonist **5**, but none of the selected scaffolds revealed to be a bioisostere of the urea function. Although compounds (*S*)-**9a**, (*S*)-**12a,** and (*S*)-**16b** showed promising in vitro anti-inflammatory and pro-resolving effects, their interaction with efflux pumps could limit CNS exposure and, thus, their potential application in in vivo models of neurodegenerative disorders. Further structural modifications will be needed to achieve a drug-like pharmacokinetic profile.

4. METHODS

4.1. Chemistry.

All chemicals were obtained from commercial suppliers (Sigma-Aldrich, Alfa Aesar, and TCI Chemicals) and used with no further purification, unless otherwise noted. Thin layer chromatography was performed with Merck plates (silica gel 60 F254). Column chromatographies were performed with a Merck silica gel 60 Å (63–200 μm) stationary phase. The silica gel/sample ratio was about 30:1 (w/w). Flash chromatography was performed on a Biotage SP1 purification system using flash cartridges prepacked with KP-Sil 32–63 μm, 60 Å silica. ^{1}H and ^{13}C NMR spectra were recorded on a 500 vnmrs500 Agilent spectrometer (500 MHz). Chemical shift values are in ppm (δ). Mass spectra were recorded with an HP6890–5973 MSD gas chromatograph/mass spectrometer. Only significant m/z peaks are reported (% of relative intensity in parentheses). High-resolution mass spectra (electrospray ionization, ESI-TOF) (HRMS) were recorded on an Agilent 6530 Accurate Mass Q-TOF (mass range 50–3000 m/z, dry gas nitrogen 10 mL/min, dry heater 325 °C, capillary voltage 4000 V, electrospray ion source in positive or negative ion mode). All mass spectra were in agreement with the structures. Target compounds elemental analyses (C,H,N) were performed on a Eurovector Euro EA 3000 analyzer. Analyses of C, H, and N were within ±0.4% of the theoretical values. RP-HPLC analysis was performed on an Agilent 1260 Infinity Binary LC System with a diode array detector using a Phenomenex Synergi Fusion-RP column (100 mm × 3 mm, 4 μm particle size). Gradient elution allowed separation of target compounds from impurities (phase A 0.01% formic acid in water, phase B 0.01% formic acid in ACN; gradient from 10% to 100% B in 10 min; flow rate: 0.7 mL/min). The purity of the target compounds was assessed by RP-HPLC and combustion analysis. All compounds exhibited ≥95% purity.

The following compounds were prepared according to the reported methods: 5-(4-fluorophenyl)-1,3,4-oxadiazol-2(3*H*)-one (**8a**),[36] 5-(4-bromophenyl)-1,3,4-oxadiazol-2(3H)-one (**8b**),[50] 5-(3-fluorophenyl)-1,3,4-oxadiazol-2(3*H*)-one (**8c**),[36] 5-(3-bromophenyl)-1,3,4-oxadiazol-2(3*H*)-one (**8d**),[51] 5-(4-methylphenyl)-1,3,4-oxadiazol-2(3*H*)-one (**8e**),[36] 5-(3-methylphenyl)-1,3,4-oxadiazol-2-(3H)-one (**8f**),[36] 2-azido-1-(4-fluorophenyl)ethan-1-one

(13),[37] 3-[(4-fluorophenyl)amino]-4-methoxycyclobut-3-ene-1,2-dione (**15a**) [37], and 3-[(4-bromophenyl)amino]-4-methoxycyclobut-3-ene-1,2-dione (**15b**).[38]

4.1.1. Procedure for the Preparation of the Isothiocyanate (R)- and (S)-10.

Thiocarbonyldiimidazole (TCDI, 1.5 mmol) was added to a stirred solution of (*R*)- or (*S*)-**7** (1.0 mmol) in anhydrous CH_2Cl_2 (10 mL). The reaction mixture was stirred at room temperature for 1–2 h. Then, the solvent was evaporated under reduced pressure, and the crude residue was purified by column chromatography using *n*-Hex/EtOAc 7:3 (v/v), as the eluent to obtain the pure compound, as detailed below.

4.1.1.1. (R)-4-[3-(Indolin-1-yl)-2-isothiocyanato-3-oxopropyl]-benzonitrile ((R)-10). Yellowish solid. Yield: 53%. ^{1}H NMR (300 MHz, $CDCl_3$): δ 3.09–3.24 (m, 2H), 3.31 (dd, 1H, J = 8.0 and 13.7 Hz), 3.41 (dd, 1H, J = 6.0 and 13.7 Hz), 3.88 (dt, 1H, J = 6.6 and 10.0 Hz), 4.18 (dt, 1H J = 6.8 and 10.0 Hz), 4.51 (dd, 1H, J = 6.0 and 7.9 Hz), 7.06–7.12 (m, 1H), 7.21 (d, 2H J = 7.9 Hz), 7.41 (d, 2H J = 8.1 Hz), 7.62 (d, 2H J = 8.1 Hz), 8.21 (d, 1H J = 8 Hz) HRMS (ESI$^+$) calcd for $[(C_{19}H_{15}N_3OS)+Na]^+$: 356.0834; found, 356.0828. ESI$^+$/MS/MS $[M + Na]^+$ m/z 76 (100).

4.1.1.2. (S)-4-[3-(Indolin-1-yl)-2-isothiocyanato-3-oxopropyl]benzonitrile ((S)-10). Yellowish solid. Yield: 53%. ^{1}H NMR (300 MHz, $CDCl_3$): δ 3.09–3.24 (m, 2H), 3.31 (dd, 1H, J = 8.0 and 13.7 Hz), 3.41 (dd, 1H, J = 6.0 and 13.7 Hz), 3.88 (dt, 1H, J = 6.6 and 10.0 Hz), 4.18 (dt, 1H J = 6.8 and 10.0 Hz), 4.51 (dd, 1H, J = 6.0 and 7.9 Hz), 7.06–7.12 (m, 1H), 7.21 (d, 2H J = 7.9 Hz), 7.41 (d, 2H J = 8.1 Hz), 7.62 (d, 2H J = 8.1 Hz), 8.21 (d, 1H J = 8 Hz) HRMS (ESI$^+$) calcd for $[(C_{19}H_{15}N_3OS)+Na]^+$: 356.0834; found, 356.0828. ESI$^+$/MS/MS $[M + Na]^+$ m/z 76 (100).

4.1.2. General Procedure for the Preparation of 2-Amino-1,3,4-oxadiazole Derivatives (R)- and (S)-9a-f.

To a solution of (*R*)- or (*S*)-**7** (0.34 mmol) and the appropriate 1,3,4-oxadiazol-2(3*H*)-one derivate (0.44 mmol) in dry DMF (5 mL) were added PyBOP (0.48 mmol) and DIPEA (0.12 mL, 0.66 mmol). The reaction mixture was stirred at room temperature overnight. Then, the reaction mixture was diluted with H_2O (20 mL) and extracted with EtOAc (3 × 20 mL). The organic layers were separated and washed with brine. The collected organic layer was dried over Na_2SO_4 and concentrated in vacuo. The crude was purified by column chromatography using *n*-hexane/EtOAc, 1:1 (v/v), as the eluent to obtain the pure compound desired, as detailed below.

4.1.2.1. (R)-4-[2-[]5-(4-Fluorophenyl)-1,3,4-oxadiazol-2-yl]-amino]-3-(indolin-1-yl)-3-oxopropyl]benzonitrile ((R)-9a). White solid, 26% yield. ^{1}H NMR (500 MHz, $CDCl_3$): δ 3.00–3.07 (m, 1H), 3.17–3.23 (m, 1H), 3.27 (dd, 1H, J = 6.0 Hz and J = 13.6 Hz), 3.36 (dd, 1H, J = 7.3 Hz and J = 13.6 Hz), 3.67 (dt, 1H, J = 6.5 Hz and J = 10.2 Hz), 4.35 (dt, 1H, J = 6.2 Hz and J = 10.2 Hz), 4.96–5.01 (m, 1H), 5.80 (d, 1H, J = 9.2 Hz, D_2O exchanged), 7.08–7.11 (m, 1H), 7.12–7.16 (m, 2H), 7.20–7.24 (m, 2H), 7.38 (d, 2H, J = 8.3 Hz), 7.58 (d, 2H, J = 8.3 Hz), 7.84–7.88 (m, 2H), 8.17 (d, 1H, J = 8.0 Hz). HRMS (ESI$^-$) calcd for $[(C_{26}H_{20}FN_5O_2)–H]^-$: 452.1528; found, 452.1516. ESI$^-$/MS/MS $[M – H]^-$ m/z 116 (100).

4.1.2.2. (S)-4-[2-[[5-(4-Fluorophenyl)-1,3,4-oxadiazol-2-yl]-amino]-3-(indolin-1-yl)-3-oxopropyl]benzonitrile ((S)-9a). White solid, 30% yield. ^{1}H NMR (500 MHz, $CDCl_3$): δ 3.00–3.07 (m, 1H), 3.17–3.23 (m, 1H), 3.27 (dd, 1H, J = 6.0 Hz and J = 13.6 Hz), 3.36 (dd, 1H, J = 7.3 Hz and J = 13.6 Hz), 3.67 (dt, 1H, J = 6.5 Hz and J = 10.2 Hz), 4.35 (dt, 1H, J = 6.2 Hz and J = 10.2 Hz), 4.96–5.01 (m, 1H), 5.80 (d, 1H, J = 9.2 Hz, D_2O exchanged), 7.08–7.11 (m, 1H), 7.12–7.16 (m, 2H), 7.20–7.24 (m, 2H), 7.38 (d, 2H, J = 8.3 Hz), 7.58 (d, 2H, J = 8.3 Hz), 7.84–7.88 (m, 2H), 8.17 (d, 1H, J = 8.0 Hz). 13C NMR (126 MHz, CDCl3): δ 27.99, 29.69, 38.76, 48.12, 56.20, 111.32, 116.13, 116.31, 117.42, 118.55, 120.24, 120.27, 124.93, 125.06, 127.66, 128.05, 128.12, 130.35, 131.69, a132.39, 141.12, 141.77, 159.04, 162.20, 163.22, 168.62. HRMS (ESI^-) calcd for $[(C_{26}H_{20}FN_5O_2)–H]^-$: 452.1528; found, 452.1516. ESI^-/MS/MS $[M – H]^-$ m/z 116 (100).

4.1.2.3. (R)-4-[2-[[5-(4-Bromophenyl)-1,3,4-oxadiazol-2-yl]-amino]-3-(indolin-1-yl)-3-oxopropyl]benzonitrile ((R)-9b). Yellowish solid, 46% yield. ^{1}H NMR (300 MHz, $CDCl_3$): δ 3.03–3.23 (m, 2H), 3.27–3.41 (m, 2H), 6.79 (dt, 1H, J = 6.5 and 10.2 Hz), 4.48 (dt, 1H, J = 6.4 and 10.2 Hz), 4.96–5.00 (m, 1H), 6.95 (br s, 1H, D_2O exchanged), 7.09–7.12 (m, 1H), 7.17–7.24 (m, 2H), 7.42–7.46 (m, 4H), 7.48–7.53 (m, 2H), 7.55–7.60 (m, 2H), 8.21 (d, 1H, J = 8.1 Hz). HRMS (ESI^-) calcd for $[(C_{26}H_{20}BrN_5O_2)–H]^-$: 512.0728; found, 512.0698. ESI^-/MS/MS $[M – H]^-$ m/z 116 (100).

4.1.2.4. (S)-4-[2-[[5-(4-Bromophenyl)-1,3,4-oxadiazol-2-yl]-amino]-3-(indolin-1-yl)-3-oxopropyl]benzonitrile ((S)-9b). Yellowish solid, 19% yield. ^{1}H NMR (300 MHz, $CDCl_3$): δ 3.03–3.23 (m, 2H), 3.27–3.41 (m, 2H), 6.79 (dt, 1H, J = 6.5 and 10.2 Hz), 4.48 (dt, 1H, J = 6.4 and 10.2 Hz), 4.96–5.00 (m, 1H), 6.95 (br s, 1H, D_2O exchanged), 7.09–7.12 (m, 1H), 7.17–7.24 (m, 2H), 7.42–7.46 (m, 4H), 7.48–7.53 (m, 2H), 7.55–7.60 (m, 2H), 8.21 (d, 1H, J = 8.1 Hz). HRMS (ESI^-) calcd for $[(C_{26}H_{20}BrN_5O_2)–H]^-$: 512.0728; found, 512.0698. ESI^-/MS/MS $[M – H]^-$ m/z 116 (100).

4.1.2.5. (S)-4-[2-[[5-(3-Fluorophenyl)-1,3,4-oxadiazol-2-yl]-amino]-3-(indolin-1-yl)-3-oxopropyl]benzonitrile ((S)-9c). Yellowish solid, 15% yield. ^{1}H NMR (300 MHz, $CDCl_3$): δ 3.00–3.21 (m, 2H), 3.29 (dd, 1H, J = 6.4 and 13.6 Hz), 3.37 (dd, 1H, J = 7.2 and 13.6 Hz), 3.70 (dt, 1H, J = 6.5 and 10.2 Hz), 4.39 (dt, 1H, J = 6.3 and 10.2 Hz), 4.96–5.03 (m, 1H), 6.31 (d, 1H, J = 8.9 Hz, D_2O exchanged), 7.07–7.16 (m, 3H), 7.19–7.24 (m, 2H), 7.34–7.42 (m, 3H), 7.47–7.51 (m, 1H), 7.56–7.59 (d, 2H, J = 8.3 Hz), 8.17–8.20 (m, 1H). HRMS (ESI^-) calcd for $[(C_{26}H_{20}FN_5O_2)–H]^-$: 452.1528; found, 452.1506. ESI^-/MS/MS $[M – H]^-$ m/z 116 (100).

4.1.2.6. (S)-4-[2-[[5-(3-Bromophenyl)-1,3,4-oxadiazol-2-yl]-amino]-3-(indolin-1-yl)-3-oxopropyl]benzonitrile ((S)-9d). White solid, 31% yield. ^{1}H NMR (300 MHz, $CDCl_3$): δ 3.04–3.21 (m, 2H), 3.27 (dd, 1H, J = 6.2 and 13.4 Hz), 3.36 (dd, 1H, J = 7.1 and 13.4 Hz), 3.69 (dt, 1H, J = 6.6 and 10.3 Hz), 4.37 (dt, 1H J = 6.3 and 10.3 Hz), 4.95–5.02 (m, 1H), 6.19 (d, 1H, J = 8.8 Hz, D_2O exchanged), 7.06–7.11 (m, 1H), 7.21 (d, 2H, J = 7.7 Hz), 7.39 (d, 2H, J = 8.2 Hz), 7.57 (d, 3H, J = 8.2 Hz), 7.71–7.74 (m, 3H), 8.17 (d, 1H, J = 8.0 Hz). HRMS (ESI^-) calcd for $[(C_{26}H_{20}BrN_5O_2)–H]^-$: 512.0722; found, 512.0773. ESI^-/MS/MS $[M – H]^-$ m/z 116 (100).

4.1.2.7. (S)-4-[3-(Indolin-1-yl)-3-oxo-2-[[5-(4-methylphenyl)-1,3,4-oxadiazol-2-yl]amino]propyl]benzonitrile ((S)-9e). White solid, 18% yield. ^{1}H NMR (300 MHz, $CDCl_3$): δ 2.39 (s, 3H), 2.95–3.22 (m, 2H), 3.24–3.40 (m, 2H), 3.67 (dt, 1H, J = 6.8 and 10.1 Hz), 4.38 (dt, 1H, J = 6.4 and 10.1 Hz), 4.95–5.03 (m, 1H), 5.97 (d, 1H, J = 8.9 Hz, D_2O exchanged), 7.06–7.11 (m, 1H), 7.19–7.24 (m, 4H), 7.39 (d, 2H, J = 8.1 Hz), 7.57 (d, 2H, J = 8.1 Hz), 7.72 (d, 2H, J = 8.0 Hz), 8.18 (d, 1H, J = 8.0 Hz). HRMS (ESI^-) calcd for $[(C_{27}H_{23}N_5O_2)–H]^-$: 448.1779; found, 448.1763. ESI^-/MS/MS $[M – H]^-$ m/z 116 (100).

4.1.2.8. (S)-4-[3-(Indolin-1-yl)-3-oxo-2-[[5-(3-methylphenyl)-1,3,4-oxadiazol-2-yl]amino]propyl]benzonitrile ((S)-9f). Yellowish solid, 8% yield. ^{1}H NMR (300 MHz, $CDCl_3$): δ 2.38 (s, 3H), 3.01–3.20 (m, 2H), 3.24–3.40 (m, 2H), 3.68 (dt, 1H, J = 6.7 and 10.2 Hz), 4.38 (dt, 1H, J = 6.3 and 10.2 Hz), 4.95–5.03 (m, 1H), 6.03 (app d, 1H, D_2O exchanged), 7.06–7.11 (m, 1H), 7.19–7.24 (m, 2H), 7.27–7.31(m, 2H), 7.39 (d, 2H, J = 8.2 Hz), 7.57 (d, 2H, J = 8.2 Hz), 7.62–7.67 (m, 2H), 8.18 (d, 1H, J = 8.1 Hz). HRMS (ESI^-) calcd for $[(C_{27}H_{23}N_5O_2)–H]^-$: 448.1779; found, 448.1771. ESI^-/MS/MS $[M – H]^-$ m/z 116 (100).

4.1.3. General Procedure for the Preparation of the 2-Amino-1,3,5-thiadiazole Derivatives (R)- and (S)-12a,b.

To a solution of (*R*)- and (*S*)-**10** (0.17 mmol) in dry THF, (5 mL) DIPEA (0.20 mL, 1.15 mmol) and DMAP (0.17 mmol) were added, and the reaction mixture was stirred at room temperature for 1–2 h. Then, *para*-toluensulfonyl chloride (0.52 mmol) and 4-fluorobenzohydrazide (0.18 mmol) were added, and the resulting mixture was refluxed overnight. After cooling, the solvents were concentrated in vacuo, and the residue was taken up with H_2O (20 mL) and extracted with EtOAc (3 × 20 mL). The organic layers were collected and washed with a saturated solution of $NaHCO_3$. The organic phase was dried over Na_2SO_4 and concentrated in vacuo. The crude was purified by chromatography using CH_2Cl_2/EtOAc 8:2 (v/v), as eluent to obtain the pure compound desired, as detailed below.

4.1.3.1. (R)-4-[2-[[5-(4-Fluorophenyl)-1,3,4-thiadiazol-2-yl]-amino]-3-(indolin-1-yl)-3-oxopropyl]benzonitrile ((R)-12a). Orange solid, 35% yield. ^{1}H NMR (500 MHz, $CDCl_3$): δ 3.09–3.16 (m, 1H), 3.26–3.32 (m, 2H), 3.36 (dd, 1H, J = 6.7 Hz and J = 13.7 Hz), 3.77 (dt, 1H, J = 6.1 Hz and J = 10.3 Hz), 4.64 (dt, 1H, J = 6.6 Hz and J = 10.3 Hz), 5.18 (dd, 1H, J = 7.4 Hz and J = 15.5 Hz), 6.85 (t, 2H, J = 8.6 Hz), 7.10–7.13 (m, 1H), 7.21–7.24 (m, 2H), 7.39–7.42 (m, 2H), 7.48 (d, 2H, J = 8. Hz), 7.59 (d, 2H, J = 8.2 Hz), 7.73 (d, 1H, J = 8.6 Hz, D_2O exchanged), 8.24 (d, 1H, J = 8.1 Hz). HRMS (ESI^-) calcd for $[(C_{26}H_{20}FN_5OS)–H]^-$: 468.1300; found, 468.1290. ESI^-/MS/MS $[M – H]^-$ m/z 116 (100).

4.1.3.2. (S)-4-[2-[[5-(4-Fluorophenyl)-1,3,4-thiadiazol-2-yl]-amino]-3-(indolin-1-yl)-3-oxopropyl]benzonitrile ((S)-12a). Orange solid, 20% yield. ^{1}H NMR (500 MHz, $CDCl_3$): δ 3.09–3.16 (m, 1H), 3.26–3.32 (m, 2H), 3.36 (dd, 1H, J = 6.7 Hz and J = 13.7 Hz), 3.77 (dt, 1H, J = 6.1 Hz and J = 10.3 Hz), 4.64 (dt, 1H, J = 6.6 Hz and J = 10.3 Hz), 5.18 (dd, 1H, J = 7.4 Hz and J = 15.5 Hz), 6.85 (t, 2H, J = 8.6 Hz), 7.10–7.13 (m, 1H), 7.21–7.24 (m, 2H), 7.39–7.42 (m, 2H), 7.48 (d, 2H, J = 8.2 Hz), 7.59 (d, 2H, J = 8.2 Hz), 7.73 (d, 1H, J = 8.6 Hz, D_2O exchanged), 8.24 (d, 1H, J = 8.1 Hz). **^{13}C** NMR

(126 MHz, $CDCl_3$): δ 28.02, 38.66, 48.06, 57.34, 111.22, 115.60, 115.78, 117.45, 118.62, 125.06, 125.09, 126.55, 126.58, 127.58, 128.36, 128.43, 130.38, 131.95, 132.37, 141.78, 142.06, 158.51, 162.46, 164.45, 167.52, 170.57. HRMS (ESI^-) calcd for [($C_{26}H_{20}FN_5OS$)–H]$^-$: 468.1300; found, 468.1290. ESI^-/MS/MS [M – H]$^-$ *m*/*z* 116 (100).

4.1.3.3. (S)-4-[2-[[5-(4-Bromophenyl)-1,3,4-thiadiazol-2-yl]-amino]-3-(indolin-1-yl)-3-oxopropyl]benzonitrile ((S)-12b). A solution of (*S*)-**10** (0.08 g; 0.24 mmol), 4-bromobenzohydrazide (0.05 g; 0.24 mmol), and Et_3N (0.03 mL; 0.24 mmol) in abs EtOH (15 mL) was stirred under reflux for 24 h. After cooling, the solvent was evaporated under reduced pressure, and the crude residue was purified by column chromatography using *n*-hexane/EtOAc 1:1, (v/v), as eluent to afford the pure compound as a yellow solid (5% yield). ^1H NMR (300 MHz, $CDCl_3$): δ 2.99–3.09 (m, 1H), 3.15–3.34 (m, 3H), 3.61–3.71 (m, 1H), 4.57 (app br s, 1H), 5.32–5.37 (m, 1H), 6.90–6.97 (m, 1H), 7.06 (app t, 1H), 7.21 (d, 2H, *J* = 7.6 Hz), 7.35 (d, 2H, *J* = 8.2 Hz), 7.41–7.46 (m, 1H, D_2O exchanged), 7.50 (d, 2H, *J* = 8.2 Hz), 7.54–7.62 (m, 3H), 7.70–7.75 (m, 1H). HRMS (ESI^-) calcd for [($C_{26}H_{20}BrN_5OS$)–H]$^-$: 528.0494; found, 528.0499. ESI^-/MS/MS [M – H]$^-$ *m*/*z* 116 (100).

4.1.4. General Procedure for the Preparation of the 2-Amino-1,3,5-thiadiazole Derivatives (S)-12c,d.

A solution of (*S*)-**10** (0.24 mmol) and 3-fluorobenzohydrazide (0.24 mmol) in ACN was heated under stirring at 80 °C for 1 h and then cooled to room temperature. Then, triphenylphosphine (0.46 mmol), hexachloroethane (0.46 mmol), and DIPEA (0.76 mmol; 0.13 mL) were added, and the reaction mixture was stirred at 100 °C for 1 h. After completion of the reaction, the solvent was evaporated under reduced pressure, and the crude residue was purified by column chromatography using *n*-hexane/EtOAc 1:1(v/v), as eluent to obtain the pure compound, as detailed below.

4.1.4.1. (S)-4-(2-((5-(3-Fluorophenyl)-1,3,4-thiadiazol-2-yl)-amino)-3-(indolin-1-yl)-3-oxopropyl)benzonitrile ((S)-12c). Yellowish solid, 30% yield. ^1H NMR (300 MHz, $CDCl_3$): δ 3.00–3.16 (m, 2H), 3.25–3.32 (m, 1H), 3.38 (dd, 1H, *J* = 6.9 and 13.5 Hz), 3.80 (dt, 1H, *J* = 6.3 and 10.2 Hz), 4.58 (dt, 1H, *J* = 6.6 and 10.2 Hz), 5.18–5.26 (m, 1H), 6.67–6.75 (m, 1H), 6.93–6.99 (m, 1H), 7.11–7.14 (m, 1H), 7.20–7.24 (m, 3H), 7.28–7.33 (m, 1H), 7.37–7.41 (m, 1H, D_2O exchanged) 7.45 (d, 2H, *J* = 8.3 Hz), 7.59 (d, 2H, *J* = 8.3 Hz), 8.22 (d, 1H, *J* = 7.9 Hz). HRMS (ESI^-) calcd for [($C_{26}H_{20}FN_5OS$)–H]$^-$: 468.1300; found, 468.1281. ESI^-/MS/MS [M – H]$^-$ *m*/*z* 116 (100).

4.1.4.2. (S)-4-[2-[[5-(3-Bromophenyl)-1,3,4-thiadiazol-2-yl]-amino]-3-(indoln-1-yl)-3-oxopropyl]benzonitrile ((S)-12d). Yellowish solid, 15% yield. ^1H NMR (300 MHz, $CDCl_3$): δ 33.03–3.17 (m, 2H), 3.30–3.42 (m, 2H), 3.73 (dt, 1H, *J* = 6.4 and 10.0 Hz), 4.49 (dt, 1H, *J* = 6.4 and 10.4 Hz), 5.18–5.27 (m, 1H), 7.06–7.13 (m, 2H), 7.17–7.22 (m, 3H), 7.41–7.44 (m, 3H), 7.57–7.60 (m, 3H), 7.83 (d, 1H, *J* = 1.4 Hz), 8.19 (d, 1H, *J* = 8.3 Hz). HRMS (ESI^-) calcd for [($C_{26}H_{20}BrN_5OS$)–H]$^-$: 528.0494; found, 528.0501. ESI^-/MS/MS [M – H]$^-$ *m*/*z* 116 (100).

4.1.5. General Procedure for the Preparation of the 2-Amino-oxazole Derivatives (R)- and (S)-14.

To a solution of (*R*)- or (*S*)-**7** (0.34 mmol) in dry 1,4-dioxane (10 mL), 2-azido-1-(4-fluorophenyl)-ethan-1-one **13** (0.42 mmol) and

triphenylphosphine (0.42 mmol) were added. The reaction mixture was heated at 100 °C for at least 30 min. After cooling, the solvent was concentrated in vacuo and the crude residue was purified by flash chromatography using a gradient of elution from *n*-hexane/AcOEt 9:1 to *n*-hexane/AcOEt 1:1, to obtain the pure compound, as detailed below.

4.1.5.1. (R)-4-[2-[[5-(4-Fluorophenyl)oxazol-2-yl]amino]-3-(indolin-1-yl)-3-oxopropyl]benzonitrile ((R)-14). Yellowish oil, 10% yield.
^{1}H NMR (300 MHz, $CDCl_3$): δ 2.99–3.10 (m, 1H), 3.14–3.18 (m, 1H), 3.19–3.25 (m, 1H), 3.32 (dd, 1H, J = 7.1 and 13.5 Hz), 3.72 (dt, 1H, J = 6.6 and 10.2 Hz), 4.36 (dt, 1H, J = 6.3 and 10.2 Hz), 4.94–4.99 (m, 1H), 5.93 (br s, 1H, D_2O exchanged), 6.88 (d, 1H, J = 2.6 Hz), 6.99–7.10 (m, 3H), 7.20 (d, 2H, J = 7.8 Hz), 7.35–7.41 (m, 4H), 7.55 (d, 2H, J = 7.8 Hz), 8.18 (d, 1H, J = 7.8 Hz). HRMS (ESI^-) calcd for $[(C_{27}H_{21}FN_4O_2)–H]^-$: 451.1576; found, 451.1571. ESI^-/MS/MS $[M – H]^-$ m/z 116 (100).

4.1.5.2. (S)-4-[2-[[5-(4-Fluorophenyl)oxazol-2-yl]amino]-3-(indolin-1-yl)-3-oxopropyl]benzonitrile ((S)-14). Yellowish oil, 10% yield.
^{1}H NMR (300 MHz, $CDCl_3$): δ 2.99–3.10 (m, 1H), 3.14–3.18 (m, 1H), 3.19–3.25 (m, 1H), 3.32 (dd, 1H, J = 7.1 and 13.5 Hz), 3.72 (dt, 1H, J = 6.6 and 10.2 Hz), 4.36 (dt, 1H, J = 6.3 and 10.2 Hz), 4.94–4.99 (m, 1H), 5.93 (br s, 1H, D_2O exchanged), 6.88 (d, 1H, J = 2.6 Hz), 6.99–7.10 (m, 3H), 7.20 (d, 2H, J = 7.8 Hz), 7.35–7.41 (m, 4H), 7.55 (d, 2H, J = 7.8 Hz), 8.18 (d, 1H, J = 7.8 Hz). HRMS (ESI^-) calcd for $[(C_{27}H_{21}FN_4O_2)–H]^-$: 451.1576; found, 451.1571. ESI^-/MS/MS $[M – H]^-$ m/z 116 (100).

4.1.6. General Procedure for the Preparation of Squaramide Derivatives (R)- and (S)-16a,b. To a stirred solution of (*R*)- or (*S*)-**7** (0.17 mmol) in a mixture of dry DMF and dry MeOH, the appropriate monosquaramide derivative (**15a,b**) (0.17 mmol) and Et_3N (0.75 mL, 5.4 mmol) were added. The reaction mixture was stirred at room temperature for 5 h. Then, the solvent was evaporated under reduced pressure, and the residue was taken up with H_2O (20 mL) and extracted with EtOAc (3 × 20 mL). The organic layers were washed with brine, dried over Na_2SO_4, and concentrated in vacuo. The crude residue was purified by column chromatography using $CHCl_3$/EtOAc 1:1 (v/v), as an eluent to obtain the pure compound, as detailed below.

4.1.6.1. (R)-4-[2-[[2-[(4-Fluorophenyl)amino]-3,4-dioxocyclobut-1-en-1-yl]amino]-3-(indolin-1-yl)-3-oxopropyl]benzonitrile ((R)-16a). Yellowish solid, 38% yield. ^{1}H NMR (300 MHz, $DMSOd_6$): δ 3.18–3.18 (m, 4H), 4.07–4.17 (m, 1H), 4.20–4.29 (m, 1H), 5.33–5.40 (m, 1H), 7.02–7.07 (m, 1H), 7.17 (app q, 3H), 7.25–7.28 (m, 1H), 7.39–7.42 (m, 2H), 7.46 (d, 2H, J = 8.2 Hz), 7.74 (d, 2H, J = 8.2 Hz), 8.09 (d, 1H, J = 8.0 Hz), 8.34 (br s, 1H, D_2O exchanged), 9.95 (br s, 1H, D_2O exchanged). HRMS (ESI^-) calcd for $[(C_{28}H_{21}FN_4O_3)–H]^-$: 479.1525; found, 479.1518. ESI^-/MS/MS $[M – H]^-$ m/z 205 (100).

4.1.6.2. (S)-4-[2-[[2-[(4-Fluorophenyl)amino]-3,4-dioxocyclobut-1-en-1-yl]amino]-3-(indolin-1-yl)-3-oxopropyl]benzonitrile ((S)-16a). Yellowish solid, 33% yield. ^{1}H NMR (300 MHz, $DMSOd_6$): δ 3.18–3.18 (m, 4H), 4.07–4.17 (m, 1H), 4.20–4.29 (m, 1H), 5.33–5.40 (m, 1H), 7.02–7.07 (m, 1H), 7.17 (app q, 3H), 7.25–7.28 (m, 1H), 7.39–7.42 (m, 2H), 7.46 (d, 2H, J = 8.2 Hz), 7.74 (d, 2H, J = 8.2 Hz), 8.09 (d, 1H, J = 8.0 Hz),

8.34 (br s, 1H, D_2O exchanged), 9.95 (br s, 1H, D_2O exchanged). HRMS (ESI^-) calcd for [($C_{28}H_{21}FN_4O_3$)–H]$^-$: 479.1525; found, 479.1518. ESI^-/MS/MS [M – H]$^-$ *m*/*z* 205 (100).

4.1.6.3. (R)-4-[2-[[2-[(4-Bromophenyl)amino]-3,4-dioxocyclobut1-en-1-yl]amino]-3-(indolin-1-yl)-3-oxopropyl]benzonitrile ((R)-16b). White solid, 51% yield. ^1H NMR (300 MHz, $DMSOd_6$): δ 3.05–3.24 (m, 3H), 3.34–3.39 (m, 1H), 4.08–4.17 (m, 1H), 4.20–4.28 (m, 1H), 5.36 (br s, 1H), 7.02–7.08 (m, 1H), 7.17–7.21 (m, 1H), 7.27 (d, 1H, *J* = 7.2 Hz), 7.36 (d, 2H, *J* = 8.9 Hz), 7.44 (d, 2H, *J* = 8.2 Hz), 7.49 (d, 2H, *J* = 8.9 Hz), 7.75 (d, 2H, *J* = 8.2 Hz), 8.09 (d, 1H, *J* = 8.0 Hz), 8.30 (br s, 1H, D_2O exchanged), 9.94 (br s, 1H, D_2O exchanged). ^{13}C NMR (126 MHz, $DMSOd_6$) δ: 27.91, 29.45, 44.16, 47.92, 56.70, 110.16, 115.02, 116.90, 119.26, 120.47, 122.81, 124.74, 125.51, 127.54, 131.23, 131.67, 132.58, 132.61, 132.89, 138.81, 142.59, 142.61, 163.71, 168.39, 168.54, 180.85, 183.99. HRMS (ESI^-) calcd for [($C_{28}H_{21}FN_4O_3$)–H]$^-$: 539.0724; found, 539.0742. ESI^-/MS/MS [M – H]$^-$ *m*/*z* 264 (79), 266 (100).

4.1.6.4. (S)-4-[2-[[2-[(4-Bromophenyl)amino]-3,4-dioxocyclobut-1-en-1-yl]amino]-3-(indolin-1-yl)-3-oxopropyl]benzonitrile ((S)-16b). White solid, 58% yield. ^1H NMR (300 MHz, $DMSOd_6$): δ 3.05–3.24 (m, 3H), 3.34–3.39 (m, 1H), 4.08–4.17 (m, 1H), 4.20–4.28 (m, 1H), 5.36 (br s, 1H), 7.02–7.08 (m, 1H), 7.17–7.21 (m, 1H), 7.27 (d, 1H, *J* = 7.2 Hz), 7.36 (d, 2H, *J* = 8.9 Hz), 7.44 (d, 2H, *J* = 8.2 Hz), 7.49 (d, 2H, *J* = 8.9 Hz), 7.75 (d, 2H, *J* = 8.2 Hz), 8.09 (d, 1H, *J* = 8.0 Hz), 8.30 (br s, 1H, D_2O exchanged), 9.94 (br s, 1H, D_2O exchanged). HRMS (ESI^-) calcd for [($C_{28}H_{21}FN_4O_3$)–H]$^-$: 539.0724; found, 539.0742. ESI^-/MS/MS [M – H]$^-$ *m*/*z* 264 (79), 266 (100).

4.1.7. General Procedure for the Preparation of the 2-Indolcarboxamide Derivatives (R)- and (S)-18a–d.

(*R*)- or (*S*)-**7** (0.29 mmol) and the appropriate 1*H*-indolcarboxylic acid **17a–d** (0.24 mmol) were dissolved in dry DMF (5 mL), and PyBOP (0.36 mmol) and *N*-methyl morpholine (0.21 mL, 1.93 mmol) were added. The reaction mixture was stirred at room temperature overnight. Then, the reaction mixture was diluted with H_2O (10 mL) and extracted with EtOAc (3 × 10 mL). The organic layers were separated, washed with brine, dried over Na_2SO_4, and concentrated in vacuo. The crude residue was purified by column chromatography using CH_2Cl_2/EtOAc 8:2 (v/v), as an eluent to obtain the pure compound, as detailed below.

4.1.7.1. (R)-N-[3-(4-Cyanophenyl)-1-(indolin-1-yl)-1-oxopropan-2-yl]-1H-indole-2-carboxamide ((R)-18a). White solid, yield: 37%. ^1H NMR (300 MHz, $CDCl_3$): δ 2.95–3.17 (m, 2H), 3.26 (dd, 1H, *J* = 6.4 Hz and *J* = 13.4 Hz), 3.39 (dd, 1H, *J* = 7.3 and 13.4 Hz), 3.73 (dt, 1H, *J* = 6.6 and 10.2 Hz), 4.27 (dt, 1H, *J* = 6.4 and 10.2 Hz), 5.33 (dd, 1H, *J* = 7.2 and 14.5 Hz), 6.98 (s, 1H), 7.07–7.12 (m, 2H), 7.19–7.24 (m, 3H), 7.31–7.39 (m, 3H), 7.49–7.55 (m, 3H), 7.79 (d, 1H, *J* = 7.8 Hz, D_2O exchanged), 8.25 (d, 1H, *J* = 7.8 Hz), 9.48 (br s, 1H, D_2O exchanged). HRMS (ESI^-) calcd for [($C_{27}H_{22}N_4O_2$)–H]$^-$: 433.1770; found, 433.1661. ESI^-/MS/MS [M – H]$^-$ *m*/*z* 198 (100).

4.1.7.2. (S)–N-[3-(4-Cyanophenyl)-1-(indolin-1-yl)-1-oxopropan-2-yl]-1H-indole-2-carboxamide ((S)-18a). White solid, yield: 24%. ^1H NMR (300 MHz, $CDCl_3$): δ 2.95–3.17 (m, 2H), 3.26 (dd, 1H, *J* = 6.4 Hz and *J* = 13.4 Hz),

3.39 (dd, 1H, J = 7.3 and 13.4 Hz), 3.73 (dt, 1H, J = 6.6 and 10.2 Hz), 4.27 (dt, 1H, J = 6.4 and 10.2 Hz), 5.33 (dd, 1H, J = 7.2 and 14.5 Hz), 6.98 (s, 1H), 7.07–7.12 (m, 2H), 7.19–7.24 (m, 3H), 7.31–7.39 (m, 3H), 7.49–7.55 (m, 3H), 7.79 (d, 1H, J = 7.8 Hz, D_2O exchanged), 8.25 (d, 1H, J = 7.8 Hz), 9.48 (br s, 1H, D_2O exchanged). HRMS (ESI^-) calcd for $[(C_{27}H_{22}N_4O_2)–H]^-$: 433.1770; found, 433.1661. ESI^-/MS/MS $[M – H]^-$ m/z 198 (100).

4.1.7.3. (R)-N-[3-(4-Cyanophenyl)-1-(indolin-1-yl)-1-oxopropan-2-yl]-5-fluoro-1H-indole-2-carboxamide ((R)-18b). Yellowish solid, yield: 35%. ^1H NMR (300 MHz, $CDCl_3$): δ 3.00–3.19 (m, 2H), 3.30 (dd, 1H, J = 7.2 and 13.7 Hz), 3.38 (dd, 1H, J = 6.8 and 13.7 Hz), 3.78 (dt, 1H, J = 6.8 and 10.0 Hz), 4.34 (dt, 1H, J = 6.7 and 10.0 Hz), 5.30 (dd, 1H, J = 7.3 and 14.9 Hz), 6.88–6.89 (m, 1H), 6.93 (dd, 1H, J = 2.4 Hz and J = 9.1 Hz), 7.06–7.17 (m, 3H), 7.22–7.25 (m, 2H), 7.41 (d, 2H, J = 8.1 Hz), 7.52 (d, 2H, J = 8.1 Hz), 7.97 (d, 1H, J = 8.2 Hz), 8.26 (d, 1H, J = 8.6 Hz), 9.39 (s, 1H, D_2O exchanged). HRMS (ESI^-) calcd for $[(C_{27}H_{21}FN_4O_2)–H]^-$: 451.1576; found, 451.1567. ESI^-/MS/MS $[M – H]^-$ m/z 216 (100).

4.1.7.4. (S)–N-[3-(4-Cyanophenyl)-1-(indolin-1-yl)-1-oxopropan-2-yl]-5-fluoro-1H-indole-2-carboxamide ((S)-18b). White solid, yield: 35%. ^1H NMR (300 MHz, $CDCl_3$): δ 3.00–3.19 (m, 2H), 3.30 (dd, 1H, J = 7.2 and 13.7 Hz), 3.38 (dd, 1H, J = 6.8 and 13.7 Hz), 3.78 (dt, 1H, J = 6.8 and 10.0 Hz), 4.34 (dt, 1H, J = 6.7 and 10.0 Hz), 5.30 (dd, 1H, J = 7.3 and 14.9 Hz), 6.88–6.89 (m, 1H), 6.93 (dd, 1H, J = 2.4 Hz and J = 9.1 Hz), 7.06–7.17 (m, 3H), 7.22–7.25 (m, 2H), 7.41 (d, 2H, J = 8.1 Hz), 7.52 (d, 2H, J = 8.1 Hz), 7.97 (d, 1H, J = 8.2 Hz), 8.26 (d, 1H, J = 8.6 Hz), 9.39 (s, 1H, D_2O exchanged). ^{13}C NMR (126 MHz, $CDCl_3$): δ 27.99, 38.62, 48.09, 52.80, 103.49, 103.54, 106.24, 106.43, 111.24, 112.63, 112.70, 113.60, 113.81, 117.42, 118.57, 125.05, 125.18, 127.72, 130.25, 131.19, 131.75, 132.37, 132.93, 141.59, 141.86, 161.02, 169.21. HRMS (ESI^-) calcd for $[(C_{27}H_{21}FN_4O_2)–H]^-$: 451.1576; found, 451.1567. ESI^-/MS/MS $[M – H]^-$ m/z 216 (100).

4.1.7.5. (R)-N-[3-(4-Cyanophenyl)-1-(indolin-1-yl)-1-oxopropan-2-yl]-6-fluoro-1H-indole-2-carboxamide ((R)-18c). White solid, 58% yield. ^1H NMR (300 MHz, $CDCl_3$): δ 2.99–3.18 (m, 2H), 3.25 (dd, 1H, J = 6.3 and 13.4 Hz), 3.38 (dd, 1H, J = 7.3 and 13.4 Hz), 3.75 (dt, 1H, J = 6.6 and 10.2 Hz), 4.28 (dt, 1H, J = 6.4 and 10.2 Hz), 5.31 (dd, 1H, J = 7.2 and 14.6 Hz), 6.87–6.93 (m, 2H), 6.99–7.08 (m, 1H), 7.10–7.13 (m, 1H), 7.22 (d, 2H, J = 8.6 Hz), 7.38 (d, 2H, J = 8.3 Hz), 7.45–7.50 (m, 1H), 7.51–7.56 (m, 3H), 8.21 (d, 1H, J = 8.0 Hz), 9.38 (br s, 1H, D_2O exchanged). HRMS (ESI^-) calcd for $[(C_{27}H_{21}FNO_2)–H]^-$: 451.1576; found, 451.1564. ESI^-/MS/MS $[M – H]^-$ m/z 216 (100).

4.1.7.6. (S)–N-[3-(4-Cyanophenyl)-1-(indolin-1-yl)-1-oxopropan-2-yl]-6-fluoro-1H-Indole-2-carboxamide ((S)-18c). White solid, 46% yield. ^1H NMR (300 MHz, $CDCl_3$): δ 2.99–3.18 (m, 2H), 3.25 (dd, 1H, J = 6.3 and 13.4 Hz), 3.38 (dd, 1H, J = 7.3 and 13.4 Hz), 3.75 (dt, 1H, J = 6.6 and 10.2 Hz), 4.28 (dt, 1H, J = 6.4 and 10.2 Hz), 5.31 (dd, 1H, J = 7.2 and 14.6 Hz), 6.87–6.93 (m, 2H), 6.99–7.08 (m, 1H), 7.10–7.13 (m, 1H), 7.22 (d, 2H, J = 8.6 Hz), 7.38 (d, 2H, J = 8.3 Hz), 7.45–7.50 (m, 1H), 7.51–7.56 (m, 3H), 8.21 (d, 1H, J = 8.0 Hz), 9.38 (br s, 1H, D_2O exchanged). HRMS (ESI^-) calcd for $[(C_{27}H_{21}FN_4O_2)–H]^-$: 451.1576; found, 451.1564. ESI^-/MS/MS $[M – H]^-$ m/z 216 (100).

4.1.7.7. (R)-N-[3-(4-Cyanophenyl)-1-(indolin-1-yl)-1-oxopropan-2-yl]-5-nitro-1H-Indole-2-carboxamide ((R)-18d). Yellow solid, yield: 34%. ^{1}H NMR (300 MHz, $CDCl_3$): δ 3.12–3.27 (m, 2H), 3.35–3.45 (m, 2H), 3.94 (dt, 1H, J = 6.8 and 10.0 Hz), 4.48 (dt, 1H, J = 7.1 and 10.0 Hz), 5.29 (dd, 1H, J = 7.4 and 14.8 Hz), 7.01 (d, 1H, J = 1.4 Hz), 7.06 (d, 1H, J = 9.1 Hz), 7.16–7.21 (m, 1H), 7.28–7.32 (m, 2H), 7.49 (d, 2H, J = 8.4 Hz), 7.54 (d, 2H, J = 8.4 Hz), 7.76 (dd, 1H, J = 2.1 and 9.1 Hz), 8.19 (d, 1H, J = 2.0 Hz), 8.31 (d, 1H, J = 7.9 Hz), 8.64 (d, 1H, J = 7.8 Hz), 10.03 (s, 1H, D_2O exchanged). HRMS (ESI^-) calcd for [($C_{27}H_{21}N_5O_4$)–H]$^-$: 478.1521; found, 478.1516. ESI^-/MS/MS [M – H]$^-$ m/z 161 (94), 204 (83), 243 (100).

4.1.7.8. (S)–N-[3-(4-Cyanophenyl)-1-(indolin-1-yl)-1-oxopropan-2-yl]-5-nitro-1H-Indole-2-carboxamide ((S)-18d). Yellow solid, yield: 56%. ^{1}H NMR (300 MHz, $CDCl_3$): δ 3.12–3.27 (m, 2H), 3.35–3.45 (m, 2H), 3.94 (dt, 1H, J = 6.8 and 10.0 Hz), 4.48 (dt, 1H, J = 7.1 and 10.0 Hz), 5.29 (dd, 1H, J = 7.4 and 14.8 Hz), 7.01 (d, 1H, J = 1.4 Hz), 7.06 (d, 1H, J = 9.1 Hz), 7.16–7.21 (m, 1H), 7.28–7.32 (m, 2H), 7.49 (d, 2H, J = 8.4 Hz), 7.54 (d, 2H, J = 8.4 Hz), 7.76 (dd, 1H, J = 2.1 and 9.1 Hz), 8.19 (d, 1H, J = 2.0 Hz), 8.31 (d, 1H, J = 7.9 Hz), 8.64 (d, 1H, J = 7.8 Hz), 10.03 (s, 1H, D_2O exchanged). HRMS (ESI^-) calcd for [($C_{27}H_{21}N_5O_4$)–H]$^-$: 478.1521; found, 478.1516. ESI^-/MS/MS [M – H]$^-$ m/z 161 (94), 204 (83), 243 (100).

4.2. Stability Assays in Rat Liver Microsomes.

Metabolic stability in rat liver microsomes was assessed as previously reported[26] by incubating in 100 mM potassium phosphate buffer (pH 7.4) and at 37 °C rat liver microsomes (1.0 mg/mL microsomal protein, Tebu-Bio, Milan, Italy), test compounds (10 μM), and the NADPH regenerating system (50 mM glucose-6-phosphate, 10 unit/mL glucose-6-phosphate dehydrogenase, 10 mM NADP, final glucose-6-phosphate dehydrogenase concentration of 1 unit/mL) (Tebu-Bio, Milan, Italy). Samples were removed at specific time end points and quenched with an equal volume of cold acetonitrile containing the internal standard. To assess in vitro half-life ($t_{1/2}$), the aliquots were removed at 0, 5, 15, 30, 60, and 120 min. Test compounds incubated with microsomes without the NADPH regenerating system were included. Quenched samples were centrifuged at 4500 rpm for 15 min. The supernatants (20 μL) were analyzed by HPLC with an Agilent 1260 Infinity Binary LC System equipped with a diode array detector (chromatographic data were analyzed with the Open Lab software) and a Phenomenex Synergi Fusion-RP column (100 mm × 3 mm, 4 μm particle size). The samples were separated by gradient elution (phase A 0.01% formic acid in water, phase B 0.01% formic acid in ACN; gradient from 10% to 100% B in 10 min) at 0.7 mL/min. Quantification of concentrations was performed by measuring the area under the peak. Parent compound percent remaining after 30 min incubation was calculated with the equation

$$\%\ \text{of parent compound remaining after 30min} = C_{\text{parent}}/C_{\text{control}} \times 100$$

where C_{parent} is the test compound concentration after incubating with the microsome fraction and NADPH regenerating system and C_{control} is test compound concentration after incubating with the microsome fraction.

In vitro half-life ($t_{1/2}$) was calculated with the expression $t_{1/2} = 0.693/b$, where b is the slope found in the linear fit of the natural logarithm of the fraction remaining of the parent compound versus the incubation time. The intrinsic plasma clearance (CL_{int}) was then calculated following the equation:

$$CL_{int} = \frac{0.693}{\text{in vitro } t_{1/2}} \cdot \frac{1}{\text{mg/mL microsomal protein}}$$

4.3. Aqueous Kinetic Solubility.

The aqueous kinetic solubility was estimated in duplicate by mixing and incubating (2 h under mild shaking at 37 °C) sample solutions (5% DMSO) at a final concentration of 100 μM in 100 mM potassium phosphate buffer (pH 7.4). Solutions were filtered using 4 mm Syringe Filters (Phenomenex) and then analyzed by using an Agilent 1260 Infinity Binary LC System equipped with a diode array detector (Open Lab software was used to analyze the chromatographic data) and a Phenomenex Synergi Fusion-RP column (100 mm × 3 mm, 4 μm particle size). The samples were eluted by gradient elution (phase A water, phase B ACN; gradient from 10% to 100% B in **10** min) at 0.7 mL/min. The relative solubility was then calculated by using the recorded area values as compared to a standard calibration curve.

4.4. Molecular Modeling Methods.

Compounds' molecular skeletons were built in the (*S*) configurations, converting the relative SMILES strings to three-dimensional structures within the Maestro software package[52] and performing thereafter with Open Babel[53] a 10,000 step Steepest Descent minimization using the Universal Force Field. The human FPR2 Cryo-EM solved sequence (pdb code 7WVV) was prepared with the Protein Preparation Wizard interface of Maestro, removing the fMLFII and G_{i2} moieties and water molecules, adding hydrogen atoms, optimizing their position, and assigning the ionization states of acid and basic residues according to PROPKA prediction at pH 7.0. Electrostatic charges for protein atoms were loaded according to the AMBER UNITED force field,[54] while the *molcharge* complement of QUACPAC[55] was used in order to achieve Marsili-Gasteiger charges for the inhibitors. Affinity maps were first calculated on a 0.375 Å spaced 75 × 65 × 70 $Å^3$ rectangular box, having the barycenter on the fMLFII sequence, and the accessibility of the binding site was exploited throughout 1000 runs of Lamarckian Genetic Algorithm implemented in AUTODOCK 4.2.6[56] using the GPU-OpenCL algorithm version.[57] Explicit water contribution was considered according to the hydration force field,[58] and the population size and the number of energy evaluations figures were set to 300 and 10,000,000, respectively.

Binding poses were ranked by **ESP**, a simple energy-, similarity-, and population-based rules where **E** accounts for the free energy of binding, the energy difference between the selected pose and the relative global minimum and the ligand efficacy. **S** is the similarity as scored by the Tanimoto_Combo coefficient according to the shape matching algorithm ROCS.[59] **P** is the cluster member population. Considering the rule valid once, at least four out of five parameters are below a certain figure. In this instance, dockings were filtered by

applying the ESP rule with threshold values equal to **FEB** ≤−7.50. Δ***E***≤ 1.00. **EFF** ≤−0.200. **SIM** ≥ 0.600. **POP** ≥ 10.

The MM-GBSA sampling was achieved by minimizing ligand receptor complexes and taking into account VSGB as the solvation model and the OPLS_20,205 force field for DG energy evaluations.

MD simulations were carried out using Desmond[60] in a canonical ensemble under NPT (constant number of particles, pressure, and temperature). With a constant temperature of 300 K and pressure of 1.01325 bar, ligand–enzyme complexes were embedded around the seven transmembrane helixes (namely, residues 28–50, 62–83, 101–121, 141–162, 206–226, 243–266, and 287–306) by a prebuilt phosphatidylcholine (POPC) molecule model mimicking the membrane milieu, and the whole molecular assemblies were then enclosed in an orthorhombic box containing SPC model water molecules. 0.15 M Na^+ and Cl^- were added to simulate the physiological environment.

Before starting MD, the entire structures were passed to the default relaxing protocol, including a series of restrained minimizations and short MD runs to gradually lower the overall energy of the system, and then the simulation started with a first 100 ns equilibration stint followed by a 1000 ns trajectory for data collection, collecting hence a total of 10,000 conformations. The time step integration, calculated using the RESPA integrator, was set to 2.0 fs, and the default temperature, pressure control protocols, bonded or nonbonded interactions, and short-range and long-range electrostatic interactions cutoff values were applied.

The trajectories produced during the MD simulation were analyzed using the Simulation Event option provided in the Desmond package. The simulation was computed using an nVidia RTX A5000 GPU within the CentOS Linux environment. Drawing of the protein structures and ligands was prepared using PyMOL (http://www.pymol.org).

4.5. Biology.

4.5.1. Ca^{2+} Mobilization Assay.

As previously reported, intracellular calcium concentrations [Ca^{2+}] were measured using a FlexStation II scanning fluorometer (Molecular Devices, Sunnyvale, CA, USA).[61] The cells, suspended in Hank's balanced salt solution (HBSS) without Ca^{2+} and Mg^{2+} ($HBSS^-$) but with 10 mM HEPES, were loaded with 1.25 μg/mL Fluo-4 AM dye and incubated for 30 min in the dark at 37 °C. After dye loading, the cells were washed with $HBSS^-$ containing 10 mM HEPES, resuspended in $HBSS^+$ containing Ca^{2+}, Mg^{2+} ($HBSS^+$) and 10 mM HEPES, and aliquoted into the wells of flat-bottom, half a rea-well black microtiter plates (2×10^5 cells/well). For direct agonist activity evaluation, compounds were added from a source plate containing dilutions of test compounds in $HBSS^+$, and changes in fluorescence were recorded (λ_{ex} = 485 nm, λ_{em} = 538 nm) every 5 s for 240 s at room temperature after the automated addition of compounds. Maximum change in fluorescence during the first 3 min, expressed in arbitrary units over the baseline, was used to determine a response. Responses for FPR2 agonists were normalized to the response induced by WKYMVM (5 nM) for FPR2-HL60 cells or fMLF (5 nM) for FPR1-HL60 cells, which were assigned a value of 100%. Compounds'

inhibitory effects on FPR2-or FPR1-dependent Ca^{2+} flux were evaluated by adding the compounds to the wells (the final concentration of DMSO was 1%) with FPR2-HL60 or FPR1-HL60 cells, respectively. The samples were preincubated for 10 min, and then 5 nM fMLF (FPR1-HL60 cells) or 5 nM WKYMVM (FPR2-HL60 cells) was added. The maximal change in fluorescence, expressed as arbitrary units over the baseline, was used to determine the agonist response. Curve fitting (at least five or six points) and calculation of median effective concentration values (IC_{50}) were obtained by nonlinear regression analysis of the dose–response curves generated using Prism 9 (GraphPad Software, Inc., San Diego, CA, USA). Efficacy was determined by comparing individual responses activated by the test compounds to those induced by a positive control (5 nM WKYMVM for FPR2-HL60 cells or 5 nM *f*MLF for FPR1-HL60 cells), which was assigned a value of 100%. Compounds were classified as not active when no response was observed within the first 2 min after addition and considering the limits of efficacy <20% and EC_{50} > 50 μM.

4.5.2. Evaluation of Permeability in Caco-2 Cells. Caco-2 cells were grown in Dulbecco's high-glucose modified Eagle medium, composed of 10% fetal bovine serum (FBS), 2 mM glutamine, 100 U/mL penicillin, and 0.1 mg/mL streptomycin (all components were purchased from Euroclone, Milan, Italy). The experiment started with the preparation of the Caco-2 monolayer, which occurred by seeding the cells (20,000/well) in Millicell plates (Millipore, Milan, Italy). Cell growth was followed for 21 days by changing the medium occasionally and measuring the transepithelial electrical resistance daily using an epithelial voltohmmeter (Millicell-ERS) until a TEER value > 240 ohms × cm^2 was reached. After 21 days, the plate was washed twice with HBSS (Invitrogen). After the second wash, the wells were filled with buffer, and the plate was kept at 37 °C for 30 min. After the incubation time, the HBSS buffer was replaced with solutions of the tested compounds (final concentration 100 μM). The plates were incubated at 37 °C for 2 h. After this incubation time, the medium in each chamber was collected, and the amount of compound recovered was measured spectrophotometrically (λ = 230 nm) using a Shimadzu UV-1800 UV/vis spectrophotometer.

Standard calibration curves were prepared at the maximum absorption wavelength of each compound using PBS as solvent and were linear (r^2 = 0.999) over the range of tested concentrations (from 0.5 to 100 μM). Each compound was tested in triplicate. Data are reported as the apparent permeability (P_{app}), in units of nm/s, determined as indicated in the following equation:

$$P = \frac{V_a}{Area \cdot time} \times \frac{[drug]_{acceptor}}{[drug]_{donor}}$$

where V_a is the volume in the acceptor well, Area is the surface area of the membrane, time is the total transport time, $[drug]_{acceptor}$ is the concentration of the drug measured by UV-spectroscopy, and $[drug]_{initial}$ is the initial drug concentration in the apical (AP) or basolateral (BL) chamber.

ER was calculated using the following equation: ER = P_{app}, BA/P_{app}, and AB, where P_{app}, BA is the apparent permeability of basal-to-apical transport, and P_{app}, BA is the apparent permeability of apical-to-basal transport.

4.6. Mouse Primary Microglial Cell Cultures.

4.6.1. Animals. C57BL/6J mice were maintained under standard conditions, with the temperature set at 23 °C and a 12 h light/dark cycle (lights on at 8:00 AM). Food and water were provided ad libitum. To determine the estrous cycle phase, daily vaginal smears were collected from the female mice. On the day of proestrus, females were housed with males for 12 h, after which the presence of sperm in the vaginal smears was checked to confirm mating. Pregnant females were then left undisturbed in their home cages. These experiments were approved by the Local Ethics Committee in Kraków, Poland (approval no. 223/2023, dated November 9, 2023).

4.6.2. Cell Culture. Primary microglial cell cultures were derived from the cortices of 1–2 day old mouse pups. After decapitation, the brains were extracted and immediately placed in cold Hanks' Balanced Salt Solution (HBSS, Gibco, New York, USA) on ice. The brains were washed at least three times with HBSS (7 mL) and then transferred to 10 mL of fresh culture media consisting of Dulbecco's Modified Eagle Medium (DMEM) with GlutaMax and high glucose (4.5 g/L) (Gibco, New York, USA) on ice. The tissue was minced and incubated in HBSS-containing glucose, bovine serum albumin (Sigma-Aldrich, St. Louis, MO, USA), and HEPES (Gibco, New York, USA) with 0.025% trypsin at 37 °C for 20 min. The trypsinization was halted by adding DMEM with GlutaMax and high glucose (4.5 g/L) supplemented with 10% heat-inactivated FBS (Gibco, New York, USA). The tissue was then gently triturated to obtain a single-cell suspension. Cells were plated at a density of 3×10^5 cells/cm^2 in culture medium composed of DMEM with GlutaMax and high glucose (4.5 g/L), supplemented with 10% heat-inactivated FBS, 100 U/mL penicillin, and 0.1 mg/mL streptomycin (all from Gibco, New York, USA), in poly-L-lysinecoated 75 cm^2 culture flasks. On the ninth day in vitro (maintained at 37 °C in a 5% CO_2 atmosphere), the flasks were agitated for 1 h with a horizontal shaker at 80 rpm (37 °C). Following centrifugation, the cells were resuspended in culture medium and seeded at final densities of 1.25×10^6 cells/well in 6-well plates, 2×10^5 cells/well in 24-well plates, or 4×10^4 cells/well in 96-well plates. The purity of microglial cell cultures was assessed as previously reported.[27]

4.6.3. Cell Treatment. In all experiments, the cells were pretreated for 30 min with the FPR2 antagonist WRW4 (Alomone Laboratories, Israel) at 10 μM. Then, the test FPR2 agonist (i.e., (*S*)-**9a**, (*S*)-**12a,** or (*S*)-**16b**) at 1 μM was added for 1 h. After that, the cells were stimulated for 24 h with 0.1 μg/mL lipopolysaccharide (0111:B4; Sigma-Aldrich, St. Louis, MO, USA). Control cultures were treated with the appropriate vehicle. Preparation of the stock solutions of the compounds used for the assay was as follows: (*S*)-**9a**, (*S*)-**12a,** and (*S*)-**16b,** 1 mM in DMSO; WRW4, 1 mM in distilled water; and LPS, 1 mg/mL in PBS. The final solutions of the tested compounds were prepared in distilled water. Each experimental set of control cultures was supplemented with the appropriate vehicles. The solvent was present in the cultures at a final concentration of 0.1% (v/v).

4.6.4. Nitric Oxide Release assay. The Griess reaction was employed to measure NO (nitrite ion in solution) production from LPS-treated microglial cells, as previously reported.[27] After 24 h of treatment, an equal volume of cell culture medium and Griess reagents (Griess A, 0.1% N-1-naphthyl ethylenediamine dihydrochloride; Griess B, 1% sulfanilamide in 5% phosphoric acid) was combined in a 96-well plate, and the absorbance was read at 540 nm using an Infinite M200PRO microplate reader (TECAN, Männedorf, Switzerland). The results were normalized to the NO levels released by vehicle-treated cells (set at 100%) and expressed as a percentage of the control ±SD.

4.6.5. LDH Release Assay. To estimate cell damage 24 h after LPS treatment, LDH release was measured as previously described.[27] Cell culture supernatants were incubated with the reagent mixture according to the manufacturer's instructions (Cytotoxicity Detection Kit, Roche, Germany). Absorbance was measured at 540 nm by using an Infinite M200PRO microplate reader (TECAN, Männedorf, Switzerland). The results were normalized to the LDH activity released from vehicle-treated cells (considered as 100%) and expressed as a percentage of the control ±SD.

4.6.6. Enzyme-Linked Immunosorbent Assay (ELISA). The medium of microglial cell cultures for IL-1β, IL-6, IL-33, and IL-10 measurement was collected 24 h after LPS treatment. The protein levels of the cytokines, IL-1β (Mouse interleukin 1-beta ELISA kit), IL-33 (Mouse interleukin 33 ELISA kit), IL-6 (Mouse interleukin 6 ELISA kit), and IL-10 (Mouse interleukin 10 ELISA kit; all obtained from FineTest, Wuhan, Hubei, China) were measured using commercially available enzyme-linked immunosorbent assay kits according to the manufacturer's instructions. The detection limits were as follows: IL-1β, 7.5 pg/mL; IL-33, 9.37 pg/mL; IL-6, 9.35 pg/mL; and IL-10, 9.35 pg/mL; the precision of both intra- and interassay measurements varied depending on the specific attributes of the assay.

4.6.7. Statistical Analysis. The findings presented in this study were obtained from independent microglia cultures having an "n" of 4–6. The results for NO/LDH release are expressed as the mean ± SD percentage of the control (vehicle-treated cells). Data from the ELISA studies are reported as the mean ± SD. Comparisons between groups were made using factorial analysis of variance, followed by Duncan's post hoc test to identify differences between treatment groups. A p-value of 0.05 or less was considered statistically significant. Symbols indicate the following: *$p < 0.05$ vs control, #$p < 0.05$ vs LPS group, $ $p < 0.05$ vs FPR2 ligand + LPS.

Supplementary Material

Refer to Web version on PubMed Central for supplementary material.

ACKNOWLEDGMENTS

This work was in part supported by a grant from the Alzheimer's Association (AARG-NTF-18–565227) and National Institutes of Health IDeA Program Grant GM103474. This work was supported by #NEXTGENERATIONEU (NGEU) and funded by the Ministry of University and Research (MUR), National Recovery and Resilience Plan (NRRP), project MNESYS (PE0000006)—A Multiscale integrated approach to the study of the nervous system in health and disease (DN. 1553 11.10.2022); NextGeneration EU_PNRR_M4.C2 Investimento 1.1_PRIN P20227TATA and by the grant no. 2021/43/B/NZ4/01133, Tasks 1, 2 (OPUS22) from

National Science Centre, Poland. J.K.F. is a PhD student at Krakow School of Interdisciplinary PhD Studies (KISD).

ABBREVIATIONS

DIPEA	diisopropylethylamine
LPS	lipopolysaccharide
LXA4	lipoxin A4
MD	molecular dynamics
PyBOP	benzotriazol-1-yloxytripyrrolidinophosphonium hexafluorophosphate
RoI	resolution of inflammation
SPM	specialized pro-resolving mediator

REFERENCES

(1). Buckley CD; Gilroy DW; Serhan CN Pro-resolving lipid mediators and mechanisms in the resolution of acute inflammation. Immunity 2014, 40, 315–327. [PubMed: 24656045]

(2). Perretti M; Leroy X; Bland EJ; Montero-Melendez T Resolution pharmacology: opportunities for therapeutic innovation in inflammation. Trends Pharmacol. Sci 2015, 36, 737–755. [PubMed: 26478210]

(3). Zhang W; Xiao D; Mao Q; Xia H Role of neuroinflammation in neurodegeneration development. Signal Transduction Targeted Ther 2023, 8, 267.

(4). Peh HY; Chen J Pro-resolving lipid mediators and therapeutic innovations in resolution of inflammation. Pharmacol. Ther 2025, 265, 108753. [PubMed: 39566561]

(5). Ponce J; Ulu A; Hanson C; Cameron-Smith E; Bertoni J; Wuebker J; Fisher A; Siu K-C; Marmelat V; Adamec J; Bhatti D Role of Specialized Pro-resolving Mediators in Reducing Neuroinflammation in Neurodegenerative Disorders. Front. Aging Neurosci 2022, 14, 780811. [PubMed: 35250536]

(6). Perretti M; Godson C Formyl peptide receptor type 2 agonists to kick-start resolution pharmacology. Br. J. Pharmacol 2020, 177, 4595–4600. [PubMed: 32954491]

(7). Mastromarino M; Lacivita E; Colabufo NA; Leopoldo M GProtein coupled receptors involved in the resolution of inflammation: ligands and therapeutic perspectives. Mini-Rev. Med. Chem 2021, 20, 2090–2103.

(8). Trojan E; Bryniarska N; Leśkiewicz M; Regulska M; Chamera K; Szuster-Głuszczak M; Leopoldo M; Lacivita E; Basta-Kaim A The contribution of Formyl Peptide Receptor dysfunction to the course of neuroinflammation: a potential role in the brain pathology. Curr. Neuropharmacol 2020, 18, 229–249. [PubMed: 31629396]

(9). Ye RD; Boulay F; Wang JM; Dahlgren C; Gerard C; Parmentier M; Serhan CN; Murphy PM International union of basic and clinical pharmacology. LXXIII. Nomenclature for the formyl peptide receptor (FPR) family. Pharmacol. Rev 2009, 61, 119–161. [PubMed: 19498085]

(10). Qin C-X; Norling LV; Vecchio EA; Brennan EP; May LT; Wootten D; Godson C; Perretti M; Ritchie RH Formylpeptide receptor 2: Nomenclature, structure, signalling and translational perspectives: IUPHAR review 35. Br. J. Pharmacol 2022, 179, 4617–4639. [PubMed: 35797341]

(11). Yi X; Tran E; Odiba JO; Qin CX; Ritchie RH; Baell JB The formyl peptide receptors FPR1 and FPR2 as targets for inflammatory disorders: recent advances in the development of small-molecule agonists. Eur. J. Med. Chem 2024, 265, 115989. [PubMed: 38199163]

(12). Perretti M; Chiang N; La M; Fierro IM; Marullo S; Getting SJ; Solito E; Serhan CN Endogenous lipid- and peptide-derived anti-inflammatory pathways generated with glucocorticoid and aspirin treatment activate the lipoxin A4 receptor. Nat. Med 2002, 8, 1296–1302. [PubMed: 12368905]

(13). Cattaneo F; Parisi M; Ammendola R Distinct signaling cascades elicited by different formyl peptide receptor 2 (FPR2) agonists. Int. J. Mol. Sci 2013, 14, 7193–7230. [PubMed: 23549262]

(14). Cooray SN; Gobbetti T; Montero-Melendez T; McArthur S; Thompson D; Clark AJ; Flower RJ; Perretti M Ligand-specific conformational change of the G-protein-coupled receptor ALX/FPR2 determines proresolving functional responses. Proc. Natl. Acad. Sci. U.S.A 2013, 110, 18232–18237. [PubMed: 24108355]

(15). Chen T; Xiong M; Zong X; Ge Y; Zhang H; Wang M; Won Han G; Yi C; Ma L; Ye RD; Xu Y; Zhao Q; Wu B Structural basis of ligand binding modes at the human formyl peptide receptor 2. Nat. Commun 2020, 11, 1208. [PubMed: 32139677]

(16). Liao Q; Ye RD Structural and conformational studies of biased agonism through formyl peptide receptors. Am. J. Physiol.: Cell Physiol 2022, 322, C939–C947. [PubMed: 35385323]

(17). Busch L; Vieten S; Brödel S; Endres K; Bufe B Emerging contributions of formyl peptide receptors to neurodegenerative diseases. Biol. Chem 2022, 403, 27–41. [PubMed: 34505459]

(18). Liang W; Chen K; Gong W; Yoshimura T; Le Y; Wang Y; Wang JM The Contribution of Chemoattractant GPCRs, Formylpeptide Receptors, to Inflammation and Cancer. Front. Endocrinol 2020, 11, 17.

(19). Corminboeuf O; Leroy X FPR2/ALXR agonists and the resolution of inflammation. J. Med. Chem 2015, 58, 537–559. [PubMed: 25365541]

(20). Bürli RW; Xu H; Zou X; Muller K; Golden J; Frohn M; Adlam M; Plant MH; Wong M; McElvain M; Regal K; Viswanadhan VN; Tagari P; Hungate R Potent hFPRL1 (ALXR) agonists as potential anti-inflammatory agents. Bioorg. Med. Chem. Lett 2006, 16, 3713–3718. [PubMed: 16697190]

(21). Asahina Y; Wurtz NR; Arakawa K; Carson N; Fujii K; Fukuchi K; Garcia R; Hsu MY; Ishiyama J; Ito B; Kick E; Lupisella J; Matsushima S; Ohata K; Ostrowski J; Saito Y; Tsuda K; Villarreal F; Yamada H; Yamaoka T; Wexler R; Gordon D; Kohno Y Discovery of BMS-986235/LAR-1219: A Potent Formyl Peptide Receptor 2 (FPR2) Selective Agonist for the Prevention of Heart Failure. J. Med. Chem 2020, 63, 9003–9019. [PubMed: 32407089]

(22). García RA; Ito BR; Lupisella JA; Carson NA; Hsu MY; Fernando G; Heroux M; Bouvier M; Dierks E; Kick EK; Gordon DA; Chen J; Mintier G; Carrier M; St-Onge S; Shah H; Towne J; Bucardo MS; Ma X; Ryan CS; Wurtz NR; Ostrowski J; Villarreal FJ Preservation of Post-Infarction Cardiac Structure and Function via Long-Term Oral Formyl Peptide Receptor Agonist Treatment. JACC Basic Transl. Sci 2019, 4, 905–920. [PubMed: 31909300]

(23). Lupisella J; St-Onge S; Carrier M; Cook EM; Wang T; Sum C; Fernando G; Apgar K; Zhang R; Carson N; Snyder BJ; Ryan CS; Ma X; Dierks EA; Little S; Kick EK; Wurtz NR; Bouvier M; Héroux M; Garcia RA Molecular Mechanisms of Desensitization Underlying the Differential Effects of Formyl Peptide Receptor 2 Agonists on Cardiac Structure-Function Post Myocardial Infarction. ACS Pharmacol. Transl. Sci 2022, 5, 892–906. [PubMed: 36268126]

(24). Stalder AK; Lott D; Strasser DS; Cruz HG; Krause A; Groenen PM; Dingemanse J Biomarker-guided clinical development of the first-in-class anti-inflammatory FPR2/ALX agonist ACT389949. Br. J. Clin. Pharmacol 2017, 83, 476–486. [PubMed: 27730665]

(25). Stama ML; Ślusarczyk J; Lacivita E; Kirpotina LN; Schepetkin IA; Chamera K; Riganti C; Perrone R; Quinn MT; Basta-Kaim A; Leopoldo M Novel ureidopropanamide based Nformyl peptide receptor 2 (FPR2) agonists with potential application for central nervous system disorders characterized by neuroinflammation. Eur. J. Med. Chem 2017, 141, 703–720. [PubMed: 29102463]

(26). Mastromarino M; Favia M; Schepetkin IA; Kirpotina LN; Trojan E; Niso M; Carrieri A; Leśkiewicz M; Regulska M; Darida M; Rossignolo F; Fontana S; Quinn MT; Basta-Kaim A; Leopoldo M; Lacivita E Design, synthesis, biological evaluation, and computational studies of novel ureidopropanamides as Formyl Peptide Receptor 2 (FPR2) agonists to target the resolution of inflammation in Central Nervous System Disorders. J. Med. Chem 2022, 65, 5004–5028. [PubMed: 35257581]

(27). Tylek K; Trojan E; Leśkiewicz M; Regulska M; Bryniarska N; Curzytek K; Lacivita E; Leopoldo M; Basta-Kaim A Time-Dependent Protective and Pro-Resolving Effects of FPR2 Agonists on Lipopolysaccharide-Exposed Microglia Cells Involve Inhibition of NF-κB and MAPKs Pathways. Cells 2021, 10, 2373. [PubMed: 34572022]

(28). Trojan E; Tylek K; Leśkiewicz M; Lasoń W; Brandenburg LO; Leopoldo M; Lacivita E; Basta-Kaim A The N-Formyl Peptide Receptor 2 (FPR2) Agonist MR-39 Exhibits Anti-Inflammatory Activity in LPS-Stimulated Organotypic Hippocampal Cultures. Cells 2021, 10, 1524. [PubMed: 34204273]

(29). Tylek K; Trojan E; Leśkiewicz M; Ghafir El Idrissi I; Lacivita E; Leopoldo M; Basta-Kaim A Microglia Depletion Attenuates the Pro-Resolving Activity of the Formyl Peptide Receptor 2 Agonist AMS21 Related to Inhibition of Inflammasome NLRP3 Signalling Pathway: A Study of Organotypic Hippocampal Cultures. Cells 2023, 12, 2570. [PubMed: 37947648]

(30). Trojan E; Tylek K; Schröder N; Kahl I; Brandenburg LO; Mastromarino M; Leopoldo M; Basta-Kaim A; Lacivita E The NFormyl Peptide Receptor 2 (FPR2) Agonist MR-39 Improves Ex Vivo and In Vivo Amyloid Beta (1–42)-Induced Neuroinflammation in Mouse Models of Alzheimer's Disease. Mol. Neurobiol 2021, 58, 6203–6221. [PubMed: 34468933]

(31). Cristiano C; Volpicelli F; Crispino M; Lacivita E; Russo R; Leopoldo M; Calignano A; Perrone-Capano C Behavioral, AntiInflammatory, and Neuroprotective Effects of a Novel FPR2 Agonist in Two Mouse Models of Autism. Pharmaceuticals 2022, 15, 161. [PubMed: 35215274]

(32). Zhuang Y; Wang L; Guo J; Sun D; Wang Y; Liu W; Xu HE; Zhang C Molecular recognition of formylpeptides and diverse agonists by the formylpeptide receptors FPR1 and FPR2. Nat. Commun 2022, 13, 1054. [PubMed: 35217703]

(33). Kugler-Steigmeier ME; Friederich U; Graf U; Lutz WK; Maier P; Schlatter C Genotoxicity of aniline derivatives in various short-term tests Mutat. Res 1989, 211, 279–289178.

(34). Ronchetti R; Moroni G; Carotti A; Gioiello A; Camaioni E Recent advances in urea- and thiourea-containing compounds: focus on innovative approaches in medicinal chemistry and organic synthesis. RSC Med. Chem 2021, 12, 1046–1064. [PubMed: 34355177]

(35). Wurtz NR; Johnson JA; Viet A; Shirude PS; Baligar V; Madduri S; Cheney DL; Park H; Lupisella JA; Hsu MY; Abousleiman M; Galella MA; Aulakh D; Dierks EA; Garcia RA; Ostrowski J; Kick EK; Wexler RR Discovery of Heteroaryl Urea Isosteres for Formyl Peptide Receptor 2 Agonists. ACS Med. Chem. Lett 2022, 13, 943–948. [PubMed: 35707160]

(36). Mahy W; Willis NJ; Zhao Y; Woodward HL; Svensson F; Sipthorp J; Vecchia L; Ruza RR; Hillier J; Kjær S; Frew S; Monaghan A; Bictash M; Salinas PC; Whiting P; Vincent JP; Jones EY; Fish PV 5-Phenyl-1,3,4-oxadiazol-2(3H)-ones Are Potent Inhibitors of Notum Carboxylesterase Activity Identified by the Optimization of a Crystallographic Fragment Screening Hit. J. Med. Chem 2020, 63, 12942–12956. [PubMed: 33124429]

(37). Harris PA; Cheung M; Hunter RN; Brown ML; Veal JM; Nolte RT; Wang L; Liu W; Crosby RM; Johnson JH; Epperly AH; Kumar R; Luttrell DK; Stafford JA Discovery and evaluation of 2-anilino-5-aryloxazoles as a novel class of VEGFR2 kinase inhibitors. J. Med. Chem 2005, 48, 1610–1619. [PubMed: 15743202]

(38). Arrighi G; PuertA A; Petrini A; Hicke FJ; Nocentini A; Fernandes MX; Padrón JM; Supuran CT; Fernández-Bolaños JG; López O Squaramide-Tethered Sulfonamides and Coumarins: Synthesis, Inhibition of Tumor-Associated CAs IX and XII and Docking Simulations. Int. J. Mol. Sci 2022, 23, 7685. [PubMed: 35887037]

(39). Schepetkin IA; Kirpotina LN; Khlebnikov AI; Jutila MA; Quinn MT Gastrin-releasing peptide/neuromedin B receptor antagonists PD176252, PD168368, and related analogs are potent agonists of human formyl-peptide receptors. Mol. Pharmacol 2011, 79, 77–90. [PubMed: 20943772]

(40). Agnew-Francis KA; Williams CM Squaramides as Bioisosteres in Contemporary Drug Design. Chem. Rev 2020, 120, 11616–11650. [PubMed: 32930577]

(41). Nguyen TFG; Decker AM; Finlay DB; Langston TL; Barrus D; Glass M; Harris DL; Zhang Y Rational design of cannabinoid type-1 receptor allosteric modulators: Org27569 and PSNCBAM-1 hybrids. Bioorg. Med. Chem 2021, 41, 116215. [PubMed: 34015703]

(42). Kelly E; Bailey CP; Henderson G Agonist-selective mechanisms of GPCR desensitization. Br. J. Pharmacol 2008, 153, S379–S388. [PubMed: 18059321]

(43). Gainetdinov RR; Premont RT; Bohn LM; Lefkowitz RJ; Caron MG Desensitization of G protein-coupled receptors and neuronal functions. Annu. Rev. Neurosci 2004, 27, 107–144. [PubMed: 15217328]

(44). Faassen F; Vogel G; Spanings H; Vromans H Caco-2 permeability, P-glycoprotein transport ratios and brain penetration of heterocyclic drugs. Int. J. Pharm 2003, 263, 113–122. [PubMed: 12954186]

(45). Hitchcock SA Structural modifications that alter the P-glycoprotein efflux properties of compounds. J. Med. Chem 2012, 55, 4877–4895. [PubMed: 22506484]

(46). Zhu Y; Lin X; Zong X; Han S; Wang M; Su Y; Ma L; Chu X; Yi C; Zhao Q; Wu B Structural basis of FPR2 in recognition of Aβ42 and neuroprotection by humanin. Nat. Commun 2022, 13, 1775. [PubMed: 35365641]

(47). Schrödinger Release 2024–1: Prime; Schrödinger, LLC, New York, NY, 2025.

(48). Liy PM; Puzi NNA; Jose S; Vidyadaran S Nitric oxide modulation in neuroinflammation and the role of mesenchymal stem cells. Exp. Biol. Med 2021, 246, 2399–2406.

(49). Rao X; Hua F; Zhang L; Lin Y; Fang P; Chen S; Ying J; Wang X Dual roles of interleukin-33 in cognitive function by regulating central nervous system inflammation. J. Transl. Med 2022, 20, 369. [PubMed: 35974336]

(50). Nissink JWM; Bazzaz S; Blackett C; Clark MA; Collingwood O; Disch JS; Gikunju D; Goldberg K; Guilinger JP; Hardaker E; Hennessy EJ; Jetson R; Keefe AD; McCoull W; McMurray L; Olszewski A; Overman R; Pflug A; Preston M; Rawlins PB; Rivers E; Schimpl M; Smith P; Truman C; Underwood E; Warwicker J; Winter-Holt J; Woodcock S; Zhang Y Generating Selective Leads for Mer Kinase Inhibitors-Example of a Comprehensive Lead-Generation Strategy. J. Med. Chem 2021, 64, 3165–3184. [PubMed: 33683117]

(51). Campos KR; Chen C-Y; Foley JR; Hiller M; Jen WS; Kassim AM; Klapars A; Peresypkin AV; Rosner T; Savarin CG; Tudge M; Variankaval N; Vydra V; Zhao D;, Synthesis and crystalline forms of CB-1 antagonist/inverse agonist WO2009/54923, 2009.

(52). Schrödinger Release 2024–4: Bioluminate; Schrödinger, LLC, New York, NY, 2024.

(53). O'Boyle NM; Banck M; James CA; Morley C; Vandermeersch T; Hutchison GR Open Babel: An open chemical toolbox. J. Cheminf 2011, 3, 33.

(54). Cornell WD; Ciepak P; Bayty CI; Gould IR; Merz KM; Ferguson DM; Spellmeyer DC; Fox T; Caldwell JW; Kollman PA A second generation Force Field for the simulation of proteins, nucleic acid, and organic molecules. J. Am. Chem. Soc 1995, 117, 5179–5197.

(55). QUACPAC 2.1.0.4; OpenEye Scientific Software, Santa Fe, NM. http://www.eyesopen.com.

(56). Morris GM; Goodsell DS; Halliday RS; Huey R; Hart WE; Belew RK; Olson AJ Automated docking using a Lamarckian genetic algorithm and an empirical binding free energy function. J. Comput. Chem 1998, 19, 1639–1662.

(57). Forli S; Olson AJ A Force Field with Discrete Displaceable Waters and Desolvation Entropy for Hydrated Ligand Docking. J. Med. Chem 2012, 55, 623–638. [PubMed: 22148468]

(58). El Khoury L; Santos-Martins D; Sasmal S; Eberhardt J; Bianco G; Ambrosio FA; Solis-Vasquez L; Koch A; Forli S; Mobley DL Comparison of affinity ranking using AutoDock-GPU and MM-GBSA scores for BACE-1 inhibitors in the D3R Grand Challenge 4. J. Comput. Aided Mol. Des 2019, 33, 1011–1020. [PubMed: 31691919]

(59). ROCS 3.4.0.4; OpenEye Scientific Software, Santa Fe, NM. http://www.eyesopen.com.

(60). Desmond Molecular Dynamics System D.E. Shaw Research, New York, NY, USA, 2023;Maestro–Desmond Interoperability Tools, Schrödinger, New York, NY, USA, 2024.

(61). Mastromarino M; Kirpotina LN; Schepetkin IA; Quinn MT; Lacivita E; Leopoldo M Aurantiamide-related dipeptide derivatives are formyl peptide receptor 1 antagonists. Medchemcomm 2019, 10, 2078–2088. [PubMed: 32206242]

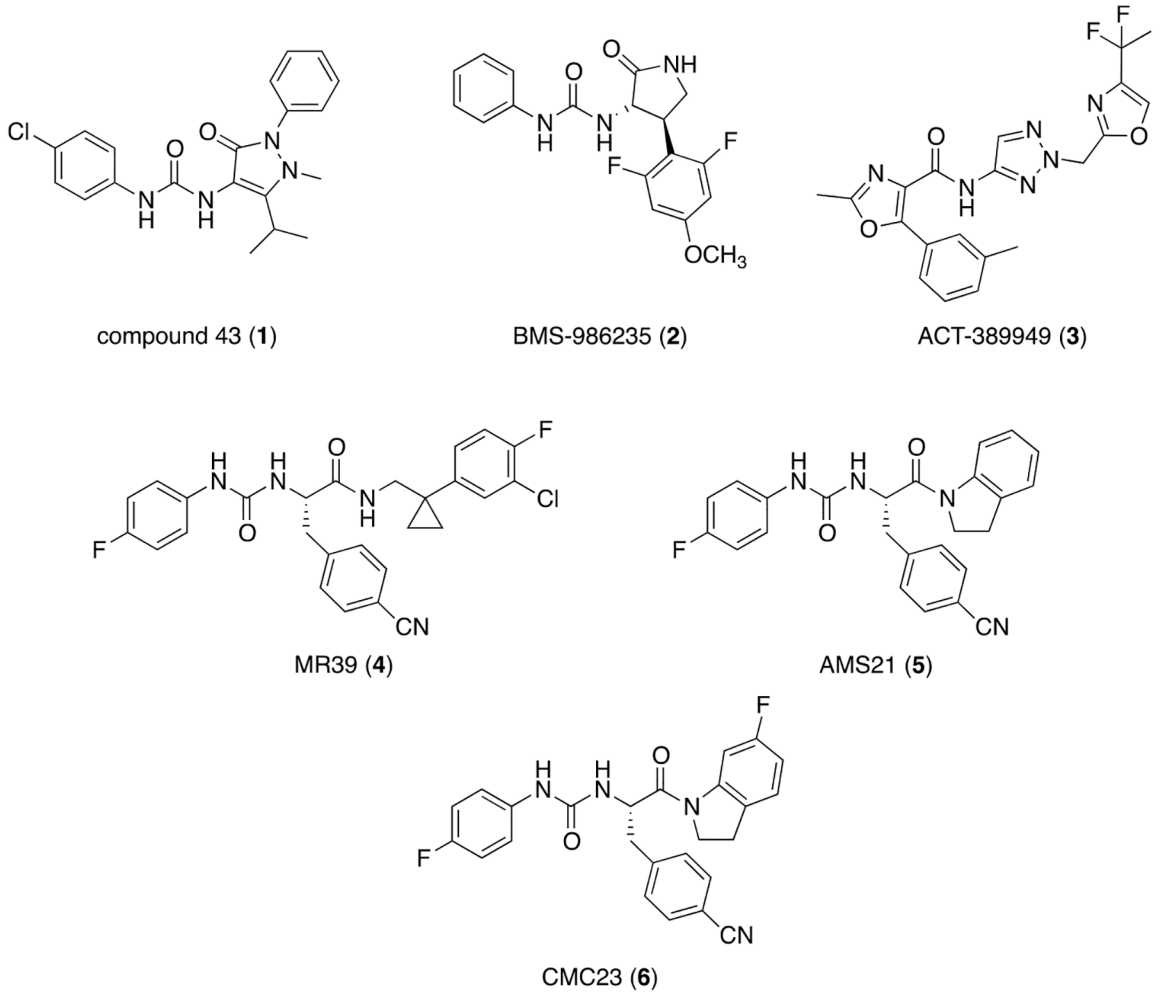

Figure 1.
Small-molecule FPR2 agonists with anti-inflammatory and pro-resolving properties.

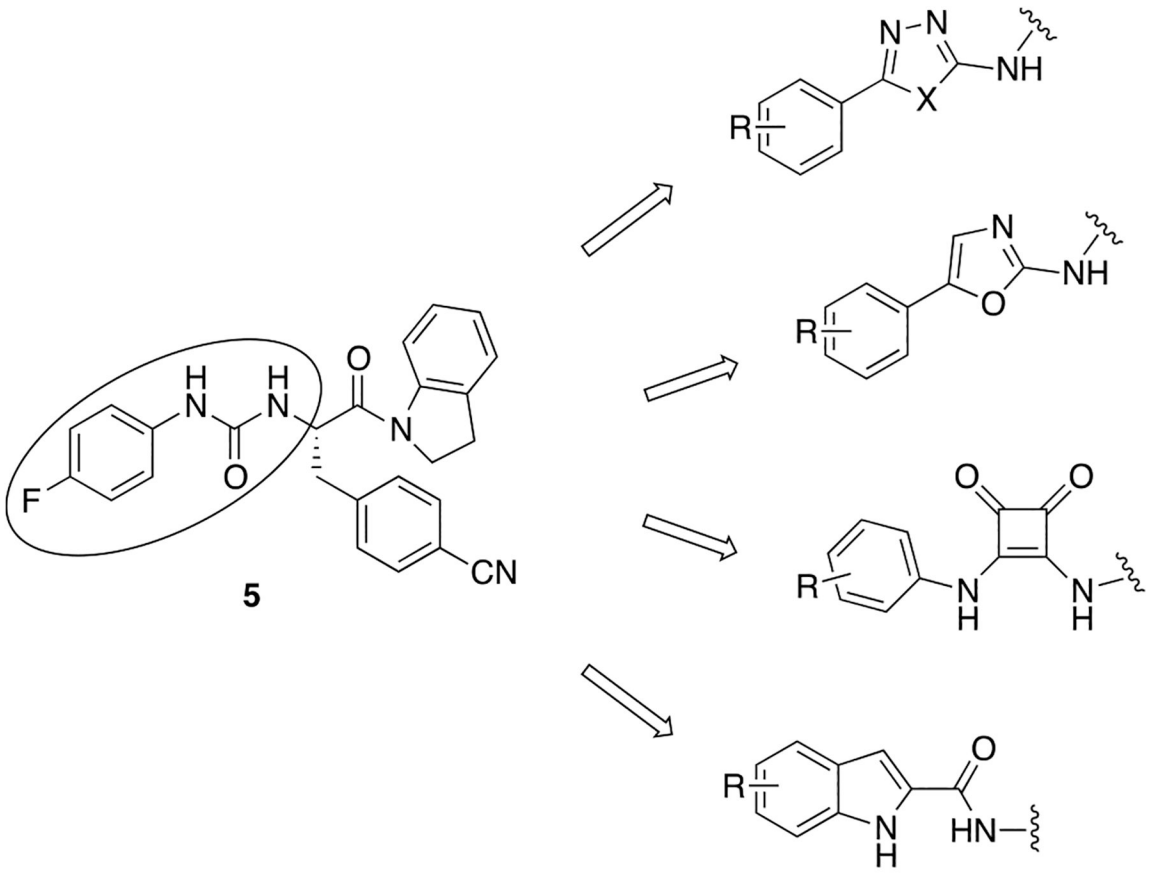

Figure 2.
Bioisosteric replacements of the phenyl urea function exploited in this study.

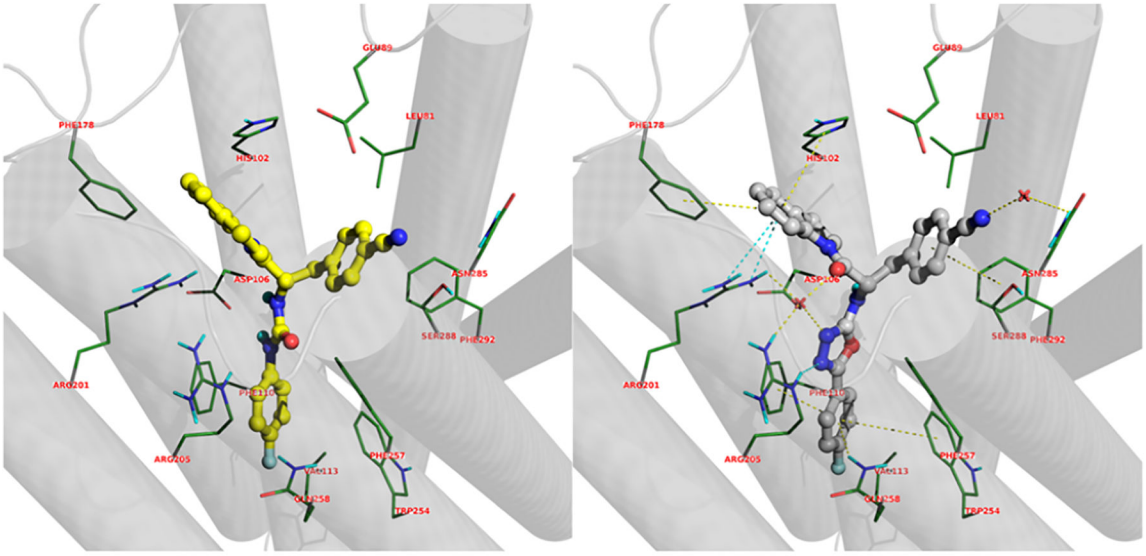

Figure 3.

Binding mode of compound **5** (yellow, left) and (*S*)-**9a** (gray, right) to the FPR2. For compound (*S*)-**9a** dashed yellow and cyan lines indicate aromatic stackings and indicate polar interactions with receptor binding site, respectively.

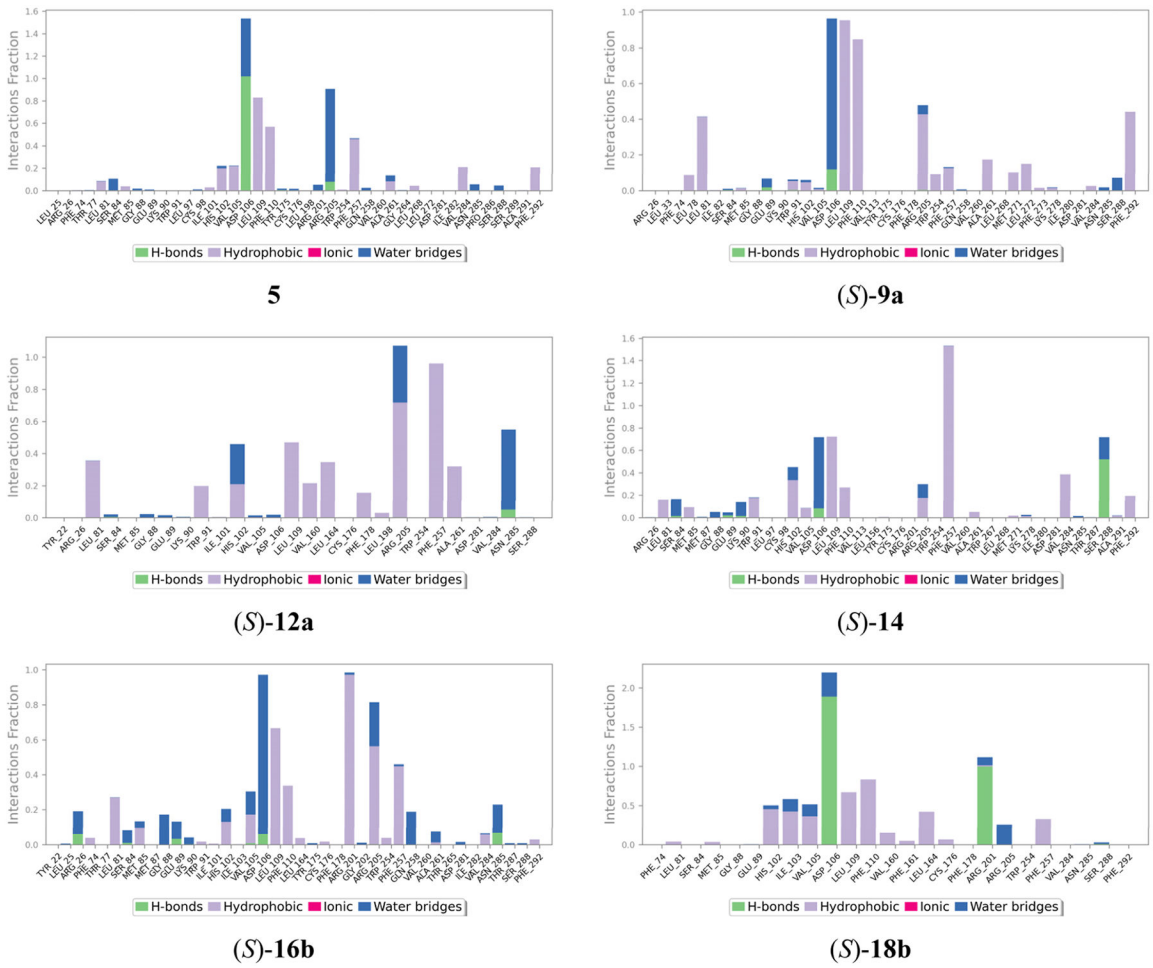

Figure 4.
Histogram plots of receptor–ligands contacts frequency extracted from the MD.

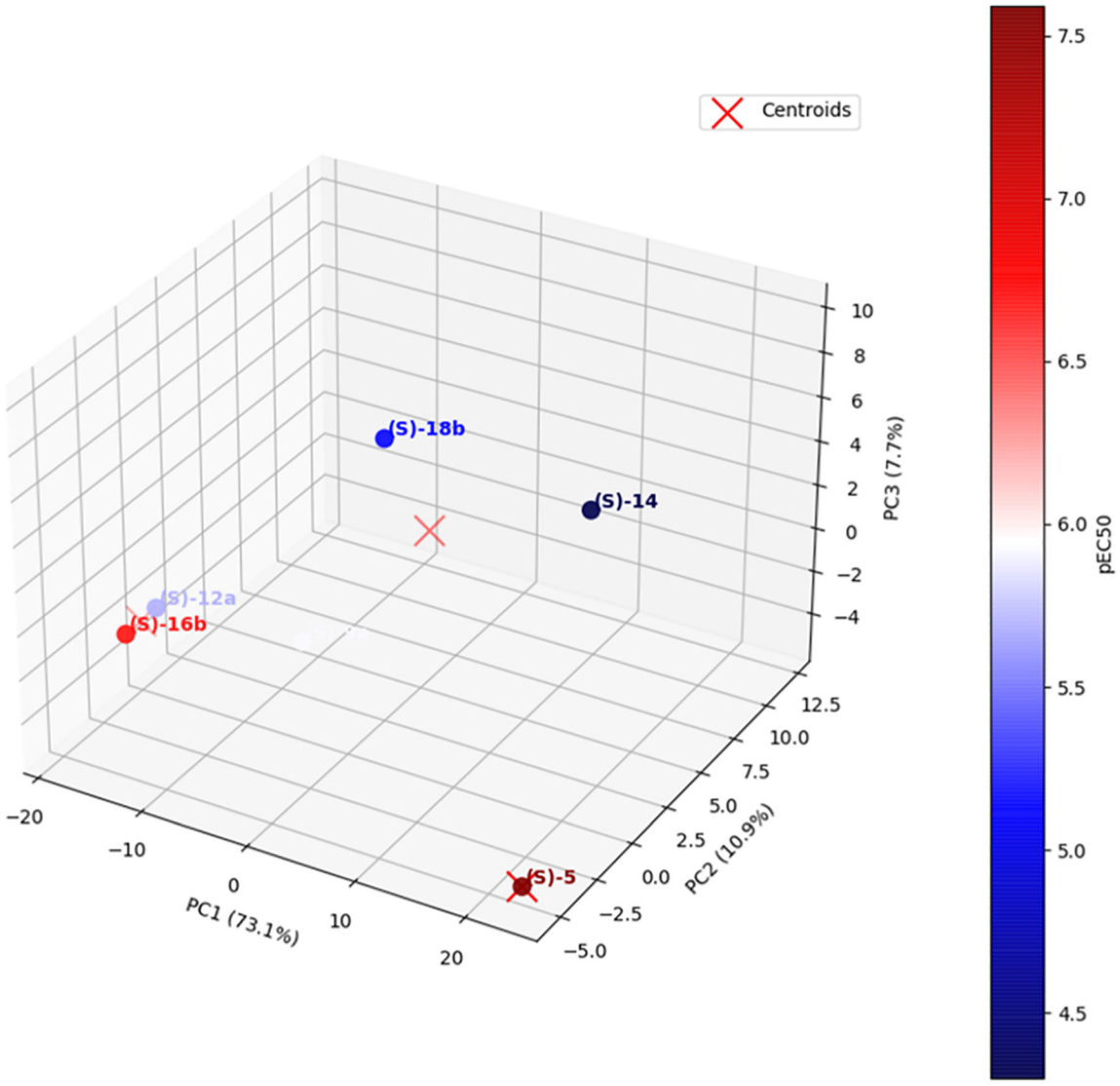

Figure 5.

3D and K-means Clustering PCA score plots. Compounds clusters are colored according to pEC_{50}. The percentage of explained variance is reported for each PC.

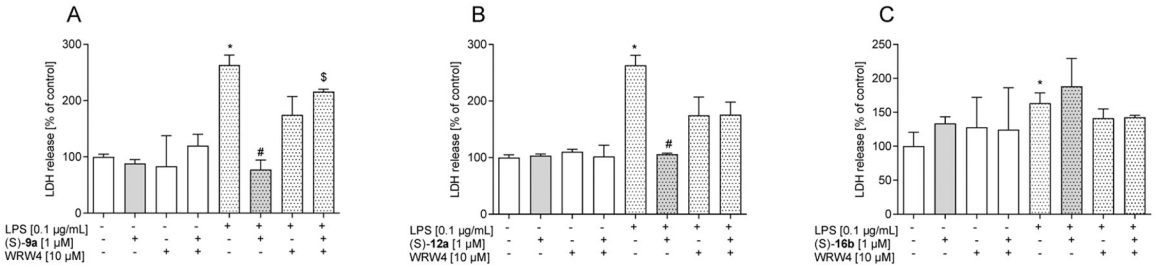

Figure 6.

Impact of the FPR2 agonists (*S*)-**9a** (A), (*S*)-**12a** (B), and (*S*)-**16b** (C) on cell death in primary microglial cells (LDH assay). The results are expressed as the mean ± SD percentage of the control (vehicle-treated cells). *$p < 0.05$ vs control, #$p < 0.05$ vs LPS group, $ $p < 0.05$ vs FPR2 ligand + LPS.

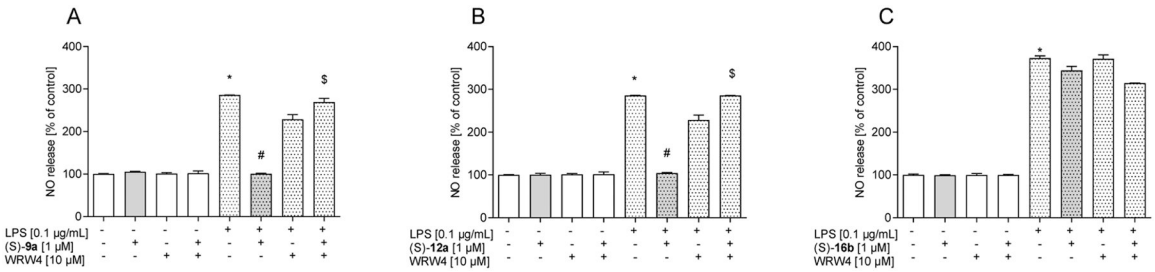

Figure 7.

Impact of the FPR2 agonists (*S*)-**9a** (A), (*S*)-**12a** (B), and (*S*)-**16b** (C) on NO release in primary microglial cells. The results are expressed as the mean ± SD percentage of the control (vehicle-treated cells). *$p < 0.05$ vs control, #$p < 0.05$ vs LPS group, $ $p < 0.05$ vs FPR2 ligand + LPS.

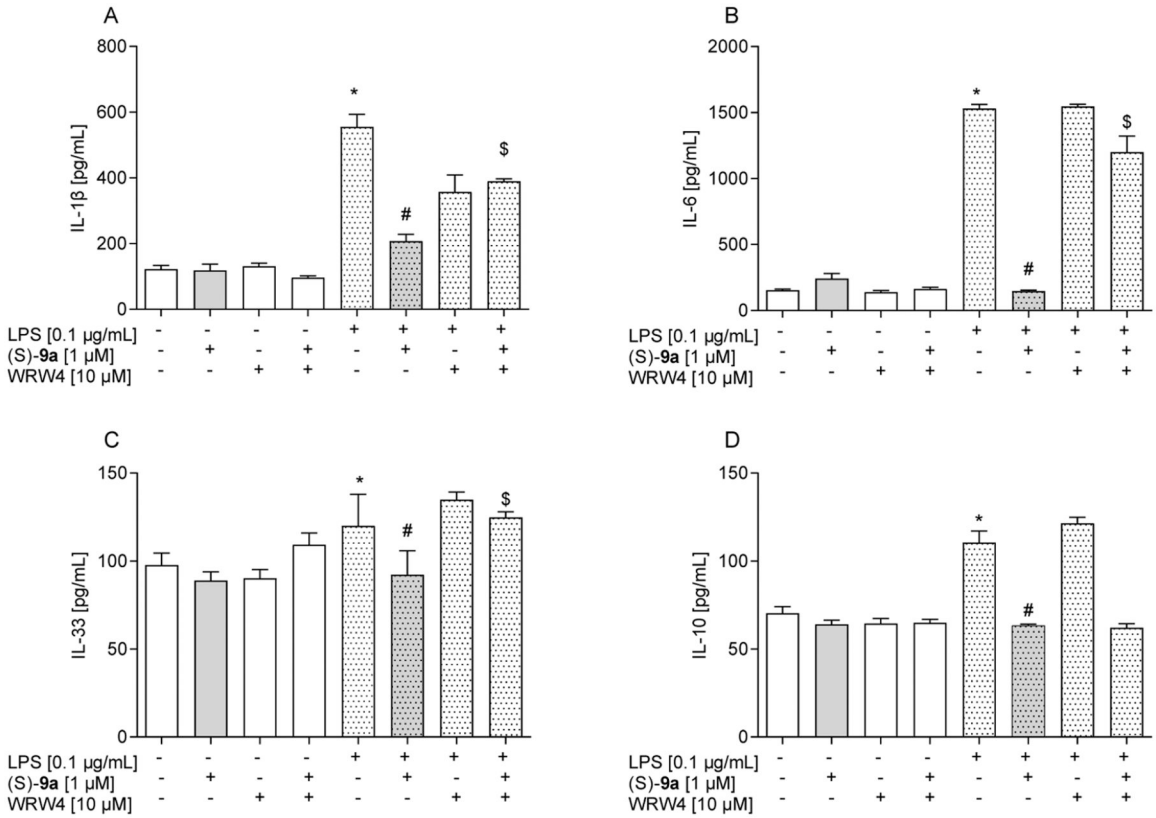

Figure 8.

Effect of (*S*)-**9a** on the level of interleukin 1*β* (IL-1*β*; A) interleukin 6 (IL-6; B), interleukin 33 (IL-33; C), and on interleukin 10 (IL-10; D) in primary microglial cells. Error bars are standard deviations. **p* < 0.05 vs control, #*p* < 0.05 vs LPS group, $ *p* < 0.05 vs FPR2 ligand + LPS.

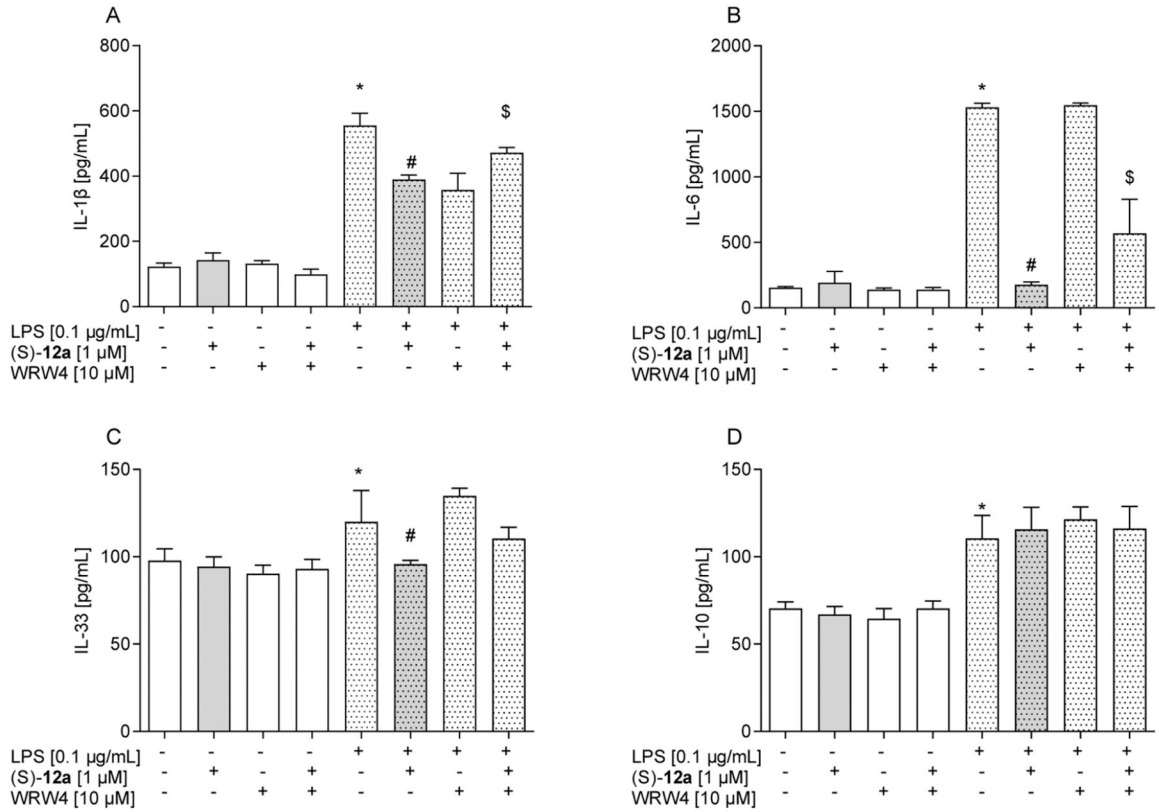

Figure 9.

Effect of (*S*)-**12a** on the level of interleukin 1β (IL-1β; A) interleukin 6 (IL-6; B), interleukin 33 (IL-33; C), and on interleukin 10 (IL-10; D) in primary microglial cells. Error bars are standard deviations. *$p < 0.05$ vs control, #$p < 0.05$ vs LPS group, $ $p < 0.05$ vs FPR2 ligand + LPS.

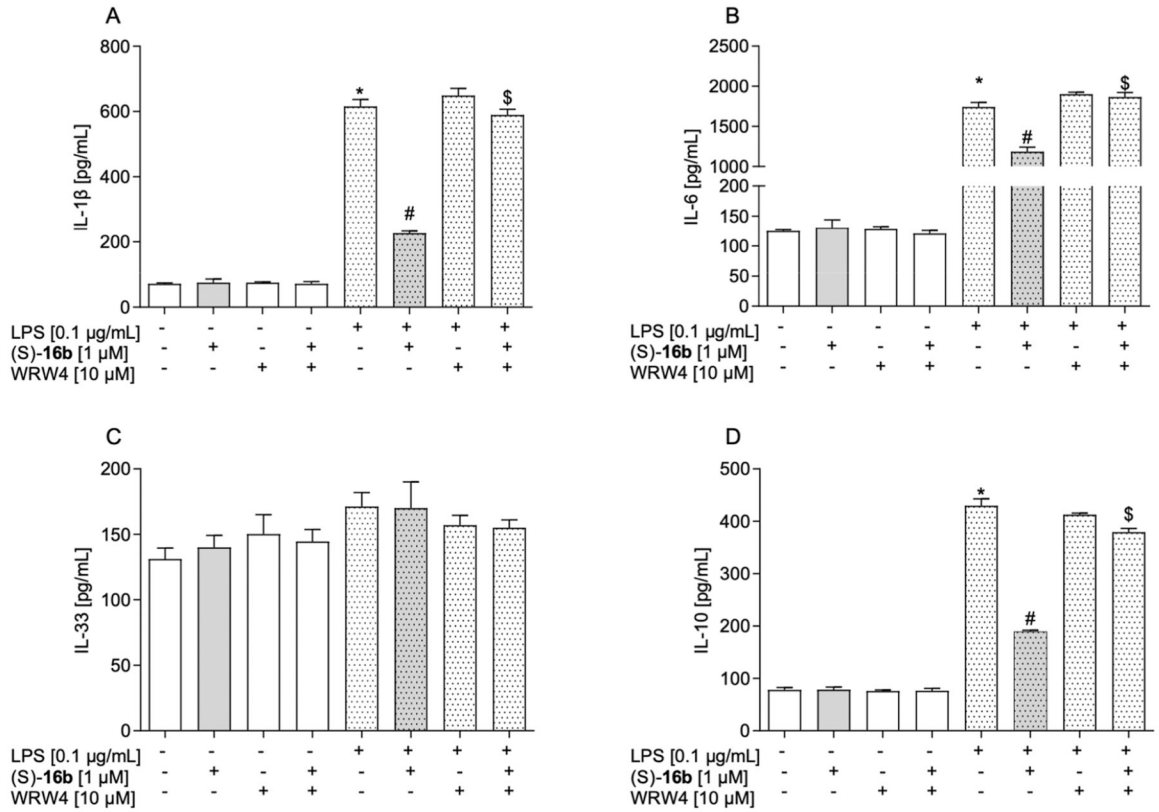

Figure 10.

Effect of (*S*)-**16b** on the level of interleukin 1β (IL-1β; A) interleukin 6 (IL-6; B), interleukin 33 (IL-33; C), and on interleukin 10 (IL-10; D) in primary microglial cells. Error bars are standard deviations. * $p < 0.05$ vs control, #$p < 0.05$ vs LPS group, $ $p < 0.05$ vs FPR2 ligand + LPS.

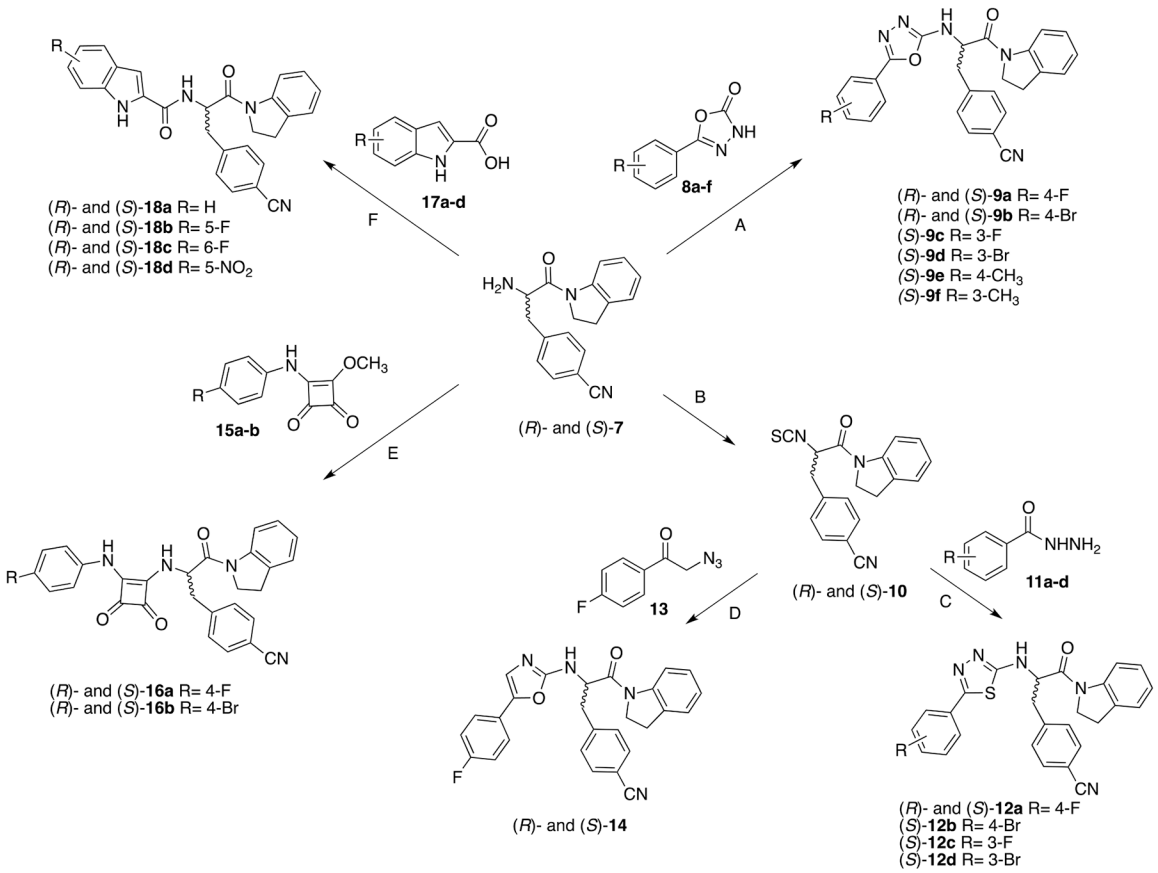

Scheme 1[a]

[a]Reagents and Conditions: (A) PyBOP, DIPEA, DMF, r.t., o.n., 8–46% yield; (B) TCDI, THF, r.t., 1–2 h, 53% yield; (C) *p*-toluenesulfonyl chloride, DMAP, DIPEA, ACN, from r.t. to reflux, o.n., 20–24% yield; or ACN, 80 °C, 1 h, then C_2Cl_6, PPh_3, DIPEA, 100 °C, 1 h, 15–30% yield; or Et_3N, EtOH, reflux, 24 h, 5% yield; (D) PPh_3, THF, 100 °C, 30 min, 10–20% yield; (E) Et_3N, MeOH, DMF, r.t., 5 h, 33–58% yield; (F) PyBOP, 4-methylmorpholine, DMF, r.t., o.n., 25–58% yield.

Table 1.

Effect of the Target Compounds on Ca^{2+} Mobilization (EC_{50}) and FPR2 and FPR1 Desensitization (IC_{50}) in FPR2- and FPR1-HL60 Transfected Cells and hPMN[a,b,c]

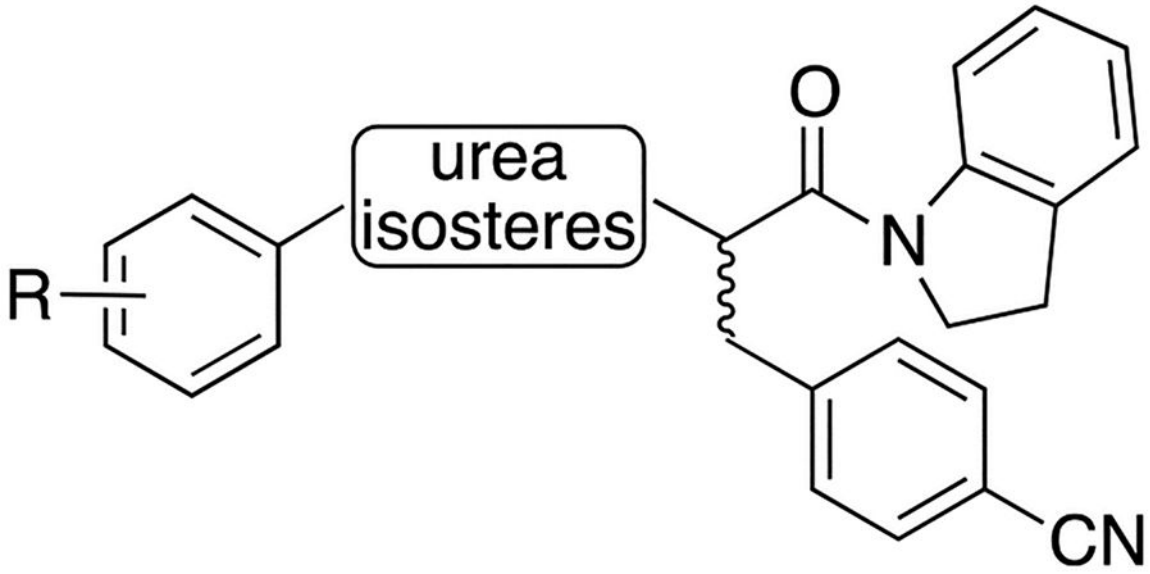

Compd	R	Urea isosteres	Calcium mobilization					
			FPR2-HL60		FPR1-HL60		hPMN	
			EC_{50}, μM (efficacy, %)	IC_{50}, μM	EC_{50} μM (efficacy, %)	IC_{50}, μM	EC_{50}, (μM (efficacy, %)	IC_{50}, μM
5			0.026[a]	0.01[a]	0.32[a]	17.6[a]	N.T.[b]	N.T.
(*R*)-9a	4-F	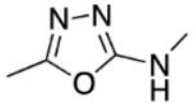	N.A.[c]	N.A.	N.A.	N.A.	N.A.	N.A.
(*S*)-9a			1.2 ± 0.4 (170)	0.32 ± 0.12	N.A.	N.A.	N.T.	N.T.
(*R*)-9b	4-Br		N.A.	N.A.	N.A.	N.A.	N.A.	N.A.
(*S*)-9b			2.0 ± 0.7 (40)	16.8 ± 3.4	2.1 ± 0.4 (40)	22.5 ± 4.9	4.3 ± 0.3 (100)	7.4 ± 2.5
(*S*)-9c	3-F		N.A.	N.A.	30.2 ± 2.9 (90)	N.A.	N.A.	N.A.
(*S*)-9d	3-Br		N.A.	N.A.	27.0 ± 6.8 (65)	N.A.	35.9 ± 9.7 (100)	N.A.
(*S*)-9e	4-CH_3		3.7 ± 1.6 (100)	1.5 ± 0.6	17.9 ± 5.5 (45)	N.A.	29.5 ± 10.8 (100)	N.A.

Compd	R	Urea isosteres	Calcium mobilization				hPMN	
			FPR2-HL60		FPR1-HL60			
			EC_{50}, μM (efficacy, %)	IC_{50}, μM	EC_{50} μM (efficacy, %)	IC_{50}, μM	EC_{50}, (μM (efficacy, %)	IC_{50}, μM
(*S*)-9f	3-CH_3		29.6 ± 3.4 (60)	N.A.	19.4 ± 5.4 (45)	N.A.	36.0 ± 10.5 (105)	N.A.
(*R*)-12a	4-F		N.A.	N.A.	N.A.	N.A.	N.A.	N.A.
(*S*)-12a			2.0 ± 0.6 (130)	0.42 ± 0.05	N.A.	N.A.	N.T.	N.T.
(*S*)-12b	4-Br		28.1 ± 3.8 (110)	37.5 ± 5.5	N.A.	N.A.	N.A.	N.A.
(*S*)-12c	3-F		37.4 ± 9.4 (105)	N.A.	N.A.	N.A.	41.4 ± 6.8 (130)	N.A.
(*S*)-12d	3-Br		13.6 ± 4.5 (140)	0.9 ± 0.3	32.9 ± 9.5 (50)	N.A.	36.3 ± 6.7 (170)	N.A.
(*R*)-14	4-F		N.A.	N.A.	N.A.	N.A.	N.A.	N.A.
(*S*)-14			N.A.	N.A.	N.A.	N.A.	N.A.	N.A.
(*R*)-16a	4-F		1.1 ± 0.4 (90)	1.1 ± 0.5	21.8 ± 4.3 (50)	N.A.	12.8 ± 2.9 (85)	N.A.
(*S*)-16a			1.0 ± 0.2 (120)	0.6 ± 0.1	16.9 ± 7.6 (40)	N.A.	0.9 ± 0.4 (120)	1.3 ± 0.4

Compd	R	Urea isosteres	Calcium mobilization				hPMN	
			FPR2-HL60		FPR1-HL60			
			EC_{50}, μM (efficacy, %)	IC_{50}, μM	EC_{50} μM (efficacy, %)	IC_{50}, μM	EC_{50}, (μM (efficacy, %)	IC_{50}, μM
(*R*)-16b	4-Br		N.A.	N.A.	32.8 ± 6.1 (60)	N.A.	N.A.	N.A.
(*S*)-16b			0.2 ± 0.1 (100)	0.2 ± 0.1	N.A.	N.A.	0.6 ± 0.3 (155)	1.2 ± 0.3
(*R*)-18a			N.A.	N.A.	N.A.	N.A.	N.A.	N.A.
(*S*)-18a			N.A.	N.A.	N.A.	N.A.	N.A.	N.A.

Compd	R	Urea isosteres	Calcium mobilization				hPMN	
			FPR2-HL60		FPR1-HL60			
			EC_{50}, µM (efficacy, %)	IC_{50}, µM	EC_{50} µM (efficacy, %)	IC_{50}, µM	EC_{50}, (µM (efficacy, %)	IC_{50}, µM
***(R)*-18b**			N.A.	N.A.	N.A.	N.A.	N.A.	N.A.
***(S)*-18b**			7.3 ± 2.1 (50)	15.7 ± 3.6	4.3 ± 0.4 (75)	4.7 ± 1.2	0.3 ± 0.2 (170)	2.6 ± 0.6
***(R)*-18c**			N.A.	N.A.	N.A.	N.A.	N.A.	N.A.
***(S)*-18c**			15.1 ± 4.8 (105)	N.A.	23.1 ± 7.6 (55)	N.A.	N.A.	N.A.

Compd	R	Urea isosteres	Calcium mobilization							
			FPR2-HL60		FPR1-HL60		hPMN			
			EC_{50}, μM (efficacy, %)	IC_{50}, μM	EC_{50} μM (efficacy, %)	IC_{50}, μM	EC_{50}, (μM (efficacy, %)	IC_{50}, μM		
(*R*)-18d			N.A.	N.A.	N.A.	N.A.	N.A.	N.A.		
(*S*)-18d			N.A.	N.A.	N.A.	N.A.	N.A.	N.A.		

[a] Data taken from ref 26.

[b] Not Tested.

[c] Not active.

Table 2.

Metabolic Stability, Kinetic Aqueous Solubility, and Permeability in Caco-2 Cells

compd	metabolic stability			kinetic aqueous solubility (μM)	permeability in Caco-2 cells		
	% of recovery after 30 min incubation	half-life (min)	Cl_{int} (μL/min/mg)		P_{app}BA (nm/s)	P_{app}AB (nm/s)	BA/AB
5	22%[a]	21[a]	33[a]	10.5	2180	493	4.4
(*S*)-**9a**	10%			4.8	2371	629	3.9
(*S*)-**9b**	29%	27	25.7	1.8			
(*S*)-**9c**	13%						
(*S*)-**9e**	18%	14	49.5	5.4			
(*S*)-**9f**	15%	18	38.5				
(*S*)-**12a**	23%	19.3	35.9	4.5	3142	112	>20
(*S*)-**12b**	25%	15	46.2				
(*S*)-**12c**	28%	47	14.7				
(*S*)-**12d**	60%	29	23.7				
(*S*)-**14**	40%	43	16.1	1.8	1996	106	19
(*R*)-**16a**	25%	15	46.2	11.8			
(*S*)-**16a**	35%	20	34.6	11.8			
(*S*)-**16b**	53%	38	18.1	9.2	2486	20	>20
(*S*)-**18b**	71%	76	9.1	1.0	3858	12	>20
(*S*)-**18c**	90%	105	6.6				

[a]Data taken from ref 26.

Table 3.

Summary of the Docking Results for the FPR2 Agonists

	FEB[a]	*AE* [b]	EFF[c]	TAN[d]	POP[e]
5	−8.52	0.00	−0.266	2.000	475/1000
(*S*)-**9a**	−7.95	0.82	−0.234	0.657	11/1000
(*S*)-**12a**	−7.95	0.97	−0.234	0.655	10/1000
(*S*)-**14**	−7.08	0.94	−0.208	0.618	10/1000
(*S*)-**16b**	−8.71	0.31	−0.242	0.682	17/1000
(*S*)-**18b**	−8.04	0.00	−0.236	0.923	48/1000

[a]FEB Free energy of binding.

[b]**ΔE** Energy difference between the selected pose and the relative global minimum.

[c]**EFF** Ligand efficacy.

[d]**TAN** Tanimoto similarity coefficient with 5 binding pose.

[e]**POP** Cluster member population.

Table 4.

Free Energy of the Docking Poses Scored by the MM-GBSA Approach

	ΔG[a]	FPR2-HL60 Calcium Mobilization EC_{50} μM	pEC_{50}
5	−62.21	0.026	7.59
(*S*)-**9a**	−64.37	1.2	5.92
(*S*)-**12a**	−61.82	2.0	5.70
(*S*)-**14**	−55.59	50	4.00
(*S*)-**16b**	−72.44	0.2	6.70
(*S*)-**18b**	−58.09	7.3	5.14

[a] kcal/mol.

Table 5.

CSA, CoM, and RoG Statistics

		mean	Sd	range
CSA [a]	**5**	500.73	31.59	137.94
	(*S*)-**9a**	510.78	31.64	138.60
	(*S*)-**12a**	509.09	29.97	121.68
	(*S*)-**14**	506.25	30.69	120.23
	(*S*)-**16b**	496.48	31.08	132.18
	(*S*)-**18b**	511.61	33.09	136.31
		Mean	**Sd**	**Range**
CoM [b]	**5**	9.75	0.64	4.22
	(*S*)-**9a**	8.92	0.34	2.97
	(*S*)-**12a**	11.49	0.41	3.04
	(*S*)-**14**	9.91	0.73	4.77
	(*S*)-**16b**	10.53	0.99	5.20
	(*S*)-**18b**	11.03	0.35	2.41
		Mean	**Sd**	**Range**
RoG [c]	**5**	21.87	0.12	0.72
	(*S*)-**9a**	21.66	0.10	0.76
	(*S*)-**12a**	21.50	0.12	0.76
	(*S*)-**14**	21.72	0.14	0.94
	(*S*)-**16b**	21.48	0.10	0.65
	(*S*)-**18b**	21.72	0.12	0.78

[a] Contact surface area in $Å^2$.

[b] Distance between ligand and receptor Center of Mass in Å.

[c] RoG in Å.